Resolving muon flux components in KM3NeT/ARCA

Master's Thesis in Physics

Presented by
Tim Kristjan Stüven

April 30, 2018

Erlangen Centre for Astroparticle Physics
Friedrich-Alexander-Universität Erlangen-Nürnberg

Supervisor: Prof. Uli Katz

Contents

Chapter 1

Introduction

KM3NeT is an extensive research infrastructure in the Mediterranean deep sea which is currently under construction. KM3NeT/ARCA is the instrument part dedicated to high-energy neutrino astronomy at the KM3NeT-Italy site off the coast of Sicily. The major goal of ARCA will be to study the origin of the high-energy astrophysical flux detected by IceCube.

The vast majority of events detected by ARCA will be down-going muons from the interactions of cosmic rays in the Earth's atmosphere. In addition, the conventional and prompt atmospheric neutrino flux, as well as the astrophysical flux, will generate incoming muons from all directions, with different energy dependencies. Studies aiming to e.g. identify the flavour composition of the astrophysical flux, or the magnitude of the prompt contribution, will need to simultaneously fit all these contributions. This work will present the results of simulations of the muon flux expected at ARCA and discuss in which regimes of energy and direction different contributions — especially those of the conventional and prompt atmospheric flux — may be disentangled.

But the atmospheric muon flux is also interesting for other reasons and not just as background signal that needs to be known in order to subtract it. Firstly, it can give information about the atmospheric muon neutrino flux since in most cases these two particles are produced together. Despite this there is no simple correlation between the two fluxes as will be discussed but there is still a lot to learn from one about the other.

Secondly, the primary flux and interaction models that can be used to simulate cosmic ray air showers are subject to large uncertainties, especially in the ultra-high energy region. The reason for this is that primary fluxes at high energies can only be measured indirectly because they are to small for measurements by spaceborne experiments. But in order to interpret the results of such indirect measurements simulations need to be run which have to rely on phenomenological interaction models. These work well up to energies where they can be compared to LHC data but uncertainties become large for the highest energies. A good measurement of the muon flux might help to reduce these uncertainties.

But after all, the focus of this work will be on the prompt component of the atmo-

spheric muon flux. The prompt flux, which is expected to exists for muons as well as muon neutrinos based on simple theoretical considerations, has not yet been measured. IceCube only gives an upper bound for the prompt atmospheric muon flux [Aar+15]. Especially since the prompt neutrino flux is expected to have a very similar steepness as the astrophysical flux, a good measurement of the former is essential to get to information about the latter and a measurement of the muon flux might give some hints on this. Thus the main question of this work is whether KM3NeT/ARCA will be able to measure the prompt muon flux.

This work is organised as follows: In chapter 2 the physical theory necessary to understand this work is introduced. This includes information about the primary cosmic ray flux, atmospheric air showers and the for this work so important cascade equation which describes showers mathematically, a section on muon production, and one about muon energy loss. In the next chapter 3 the KM3NeT/ARCA detector is explained briefly with a focus on the parameters relevant to this work. The detector is not yet build and we have to rely on simulations for the analyses. How this works will be explained in chapter 4 where first models for the primary flux, the atmosphere, and particle interactions are explained and then two very different approaches to flux calculations are introduced. In chapter 5 the results are presented.

Chapter 2

Scientific Background

This chapter gives some background information needed to fully understand the later chapters. The treatment of the topics is mostly kept at a basic level and people working in the field of neutrino astronomy can skip most parts. It is recommended though to take a look at section 2.3 where the cascade equation is introduced in a notation used again later when the numerical solver is discussed.

The muon flux this work is about is a product of atmospheric air showers which are induced by cosmic rays and thus this chapter starts with a treatment of these before atmospheric air showers themselves are discussed in the second section. Afterwards there will be a separate section about the cascade equation which is a differential equation (or rather a system of differential equations) that describes the development of air showers. Muons are the particles we are interested in here and thus there will be one section concentrating on their production followed by another discussing their energy loss.

2.1 Cosmic rays

The earth's atmosphere is constantly hit by charged particles, the cosmic rays. This was already discovered over a century ago by Victor Hess [Hes12] and numerous experiments have been conducted since in order to measure their energy spectrum and composition with an ever higher accuracy [Gru05]. Their origin, however, still remains subject to speculation.

Cosmic rays cannot be traced back to any sources because inter- and extragalactic magnetic fields are constantly changing their direction during the particles' long journey, leading to an almost isotropic distribution [PDG16]. Admittedly, the low energy flux (< 10 GeV/nucleon) is influenced by the solar- and geomagnetic field [Gru05] and the sun even contributes itself with the so called *solar energetic particles* [GER16], but this region of the spectrum is of no interest for this work.

The relevant quantity for our purpose, the calculation of muon spectra from atmospheric showers, is the spectrum of nucleons per GeV/nucleon because the production of

the hadrons who decay to muons occurs at the level of interaction between the distinct nucleons in nuclei [Gai12]. Over a wide range this spectrum can to a good approximation be described by a broken power law $E^{-\alpha}$ with $\alpha = 2.7$ below around 10^6 GeV and $\alpha = 3.1$ above, the region of transition being called the *knee* [KS12]. The low energy flux up to about 100 TeV can be measured directly using spectrometers or calorimeters carried by e.g. balloons or the ISS whereas at high energies – the ones relevant for this work – the flux becomes too small and one has to rely on indirect measurements by air shower detectors on ground [GER16]. Air showers will be discussed in the next section.

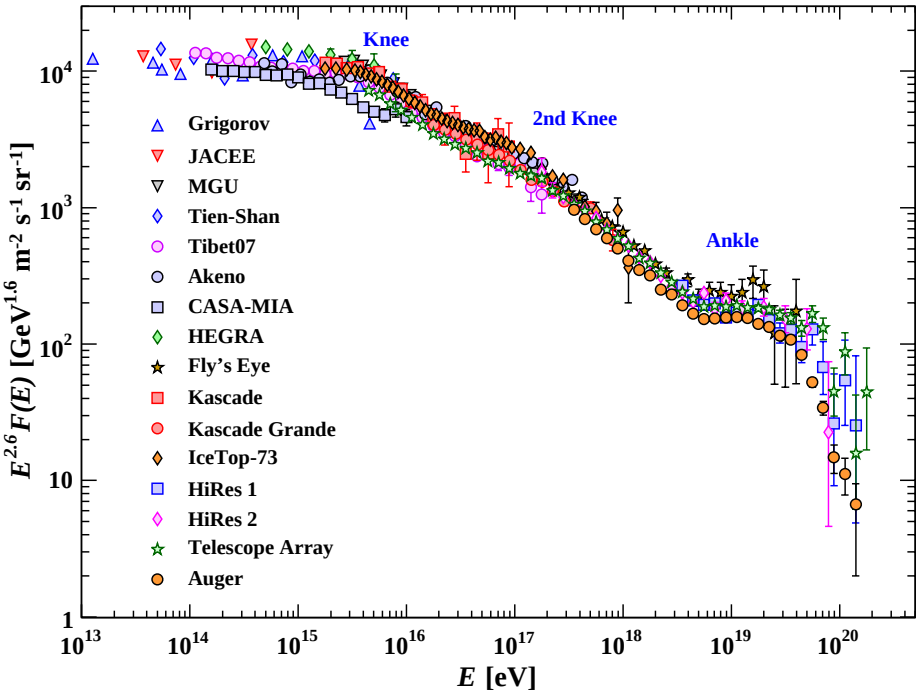

Figure 2.1: Scaled all-particle per-nucleus-energy spectrum of cosmic rays at high energies from air shower measurements. Figure taken from [PDG16].

The spectrum at high energies obtained by air shower measurements is shown in Figure 2.1 where one can see besides a less distinct second knee that at around $10^{9.5}$ GeV the spectrum flattens again to $\alpha = 2.7$, the so called *ankle*. A little before 10^{11} GeV the spectrum falls steeply and seems to be cut-off shortly after, the *GZK cut-off*. Named after its predictors Greisen, Zatsepin and Kuzmin this feature is believed to be caused by inelastic interactions of cosmic rays with the cosmic microwave background, leading

to a rapid energy loss [Gru05].

Even though the sources of cosmic rays remain unknown, there are several candidates. Most cosmic rays, especially those up the knee, are believed to originate inside the Milky Way, most likely from supernova remnants where particles can be accelerated up to energies around the knee. It is also around this energy region where charged particles cannot be kept inside the galaxy by its magnetic field which might also be a reason for the steepening of the spectrum. Other possible sources within the galaxy are pulsars and binary systems with a neutron star or a black hole. Above the ankle the flux is believed to almost completely be of extragalactic origin, candidates being Active Galactic Nuclei, Gamma Ray Bursts and star burst galaxies [KS12].

Particles originating directly from the sources described above include all nuclei produced in stellar nucleosynthesis, the largest fraction being protons and α-particles which are making up for about 90% and 9% of the total flux of nuclei (or 70% and 18% of the total flux of nucleons) respectively, as well as electrons. In this context, these are called *primaries*. They might interact with the interstellar medium, thereby producing other particles like lithium, beryllium, and boron, leading to what are called *secondary* cosmic rays; to the end that the earth will be hit by all kinds of stable particles and nuclei [PDG16]. The flux of electrons and positrons is much lower and their spectrum falls steeper compared to the hadronic component and thus only the latter will be taken into account in the following. It is difficult to determine the composition with indirect air shower measurements because of large shower to shower fluctuations that smear out differences which in principle are arising from a different primary composition.

According to Peters [Pet61], the knee and other features of the spectrum appear at different energies for different particles because they are assumed to depend on the magnetic rigidity

$$R = \frac{pc}{Ze} \tag{2.1}$$

which determines the gyroradius of a particle in a magnetic field B via $r_L = R/B$. Peters then assumes there to be a characteristic rigidity R_c at which the acceleration process reaches a limit, e.g. because the gyroradius exceeds the accelerator size. Because of this a feature in the flux should show at a characteristic energy

$$E_{tot,c} = A \cdot E_{N,c} Ze \cdot R_c \tag{2.2}$$

where E_N is the energy per nucleon and A the atomic mass, i.e. first for protons, then for α-particles followed by the heavier nuclei. Observational hints for this rigidity dependence were found e.g. by the KASCADE-Grande experiment [Ape+11].

Whether a cosmic ray is of primary or secondary origin is of no importance for the rest of this work and we will drop this distinction, giving everything described in this section the attribute *primary*. When it is written of *secondary* cosmic rays in the following, particles produced by the interaction of primaries with nuclei in the earth's atmosphere are meant.

2.2 Atmospheric air shower

When high energy cosmic rays hit the atmosphere they induce a so called atmospheric air shower. We distinguish between two different types: hadronic and electromagnetic air showers. The latter are induced by electrons, positrons or gamma rays and also appear as sub-showers of the former. In principle muons can be produced in electromagnetic showers by conversion of a photon into a pair of muons ($\gamma + Z \rightarrow \mu^+\mu^- + Z$) but the contribution to the total atmospheric muon flux is about one order of magnitude smaller than than what is produced by meson decay, happening in hadronic showers [Ill+11]. Only those are accounted for in the calculations to follow and to those we will restrict our theoretical treatment.

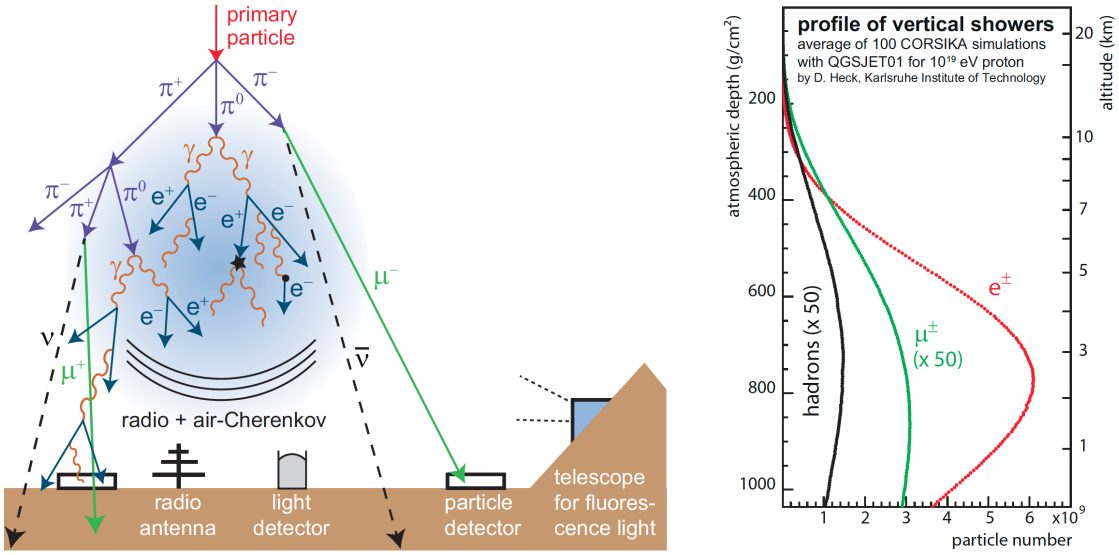

Figure 2.2: Left: Sketch of an air shower with only a few types of particles produced shown. Right: Longitudinal profile for different particle types for a shower with zenith angle $\theta = 0$. Figure taken from [Sch17].

As sketched in Figure 2.2, a hadronic air shower, once started by the interaction of a cosmic ray particle with an air nucleus, has a core of high-energy hadrons which permanently inject new hadronic and electromagnetic sub-showers. The latter are a product of neutral pions which are decaying mainly via $\pi^0 \rightarrow 2\gamma$ [Gru05]. The interesting components for us are the hadrons which can decay to muons. At low energies these are mainly pions and kaons and they make up what is called the *conventional* muon flux. At high energies, i.e. longer lifetimes, they are more and more likely to interact again instead of decaying and the muon flux becomes dominated by those which are produced in the decay of heavier mesons, containing a charm or bottom quark, or unflavoured ones. The muon flux from this origin is called the *prompt* flux and the part it plays in the muon spectrum at KM3NeT/ARCA is the main topic of this thesis. We will come back to it in section 2.4.

2.3 The cascade equation

The flux of a particle h in the atmosphere can be described by the cascade equation which is presented here directly in the form for a discrete energy bin E_i that will later serve as the starting point for a numerical solution, closely following [Fed+15]:

$$\frac{\mathrm{d}\Phi^h_{E_i}}{\mathrm{d}X} = -\frac{\Phi^h_{E_i}}{\lambda^h_{int,E_i}} \tag{2.3a}$$

$$-\frac{\Phi^h_{E_i}}{\lambda^h_{dec,E_i}(X)} \tag{2.3b}$$

$$+\sum_{E_k \geq E_i}\sum_l \frac{c_{l(E_k)\to h(E_i)}}{\lambda^l_{int,E_k}}\Phi^l_{E_k} \tag{2.3c}$$

$$+\sum_{E_k \geq E_i}\sum_l \frac{d_{l(E_k)\to h(E_i)}}{\lambda^l_{dec,E_k}(X)}\Phi^l_{E_k}. \tag{2.3d}$$

It describes the change in the particle flux Φ as a function of the atmospheric slant depth which is defined as

$$X(h_O) = \int_0^{h_O} \mathrm{d}l\,\rho_{air}(h_{atm}(l)) \tag{2.4}$$

where h_O is the observation height and ρ_{air} the air density, depending on the local height h_{atm}. The integration is carried out along the trajectory l which depends on the zenith angle and starts at the top of the atmosphere. For zenith angle $\theta = 0°$, $l = h_{top} - h_{atm}$.

Equation 2.3a is the first of two sink terms and describes the loss of particles h in the energy bin E_i through interaction with air nuclei. λ^h_{int,E_i} is obtained by multiplying the particle's interaction length by the density, leading to a characteristic length in units of g/cm^2 [GER16]:

$$\lambda^h_{int,E_i} = \frac{\rho_{air}}{n_A \sigma^{\mathrm{inel}}_{p-air}(E_i)} = \frac{m_{air}}{\sigma^{\mathrm{inel}}_{p-air}(E_i)}. \tag{2.5}$$

The second sink term, Equation 2.3b, describes the loss of particles h in the energy bin E_i through decay and $\lambda^h_{dec,E_i}(X)$ is the characteristic length obtained by multiplying the particle's decay length with the density:

$$\lambda^h_{dec,E_i}(X) = \frac{c\tau_h E_i \rho_{air}(X)}{m_h}. \tag{2.6}$$

The equations 2.3c and 2.3d are source terms. The former describes the creation of particles h by interaction of other, higher energetic, particles with air nuclei, the latter the creation by the decay of possible parent particles.

There are two boundary conditions for the cascade equation 2.3 which are physically

of a quiet different nature [GER16]. The first one is

$$\Phi^h_{E_i}(0) = \Phi^h_{E_i}(\text{primary flux}), \tag{2.7}$$

i.e. the particle flux at the top of the atmosphere at $l = 0$ (defined as in Equation 2.4) is given by the cosmic ray primary flux which is not surprising since the primaries are what starts the cascade.
The second one is

$$\Phi^h_{E_i}(0) = A \cdot \delta \left(\Phi^h_E - \frac{\Phi^h_{E_i}(0)}{A} \right) \delta(t - t_0), \tag{2.8}$$

meaning it is assumed that primaries with mass A and energy E_0 behave like A separate nucleons with an energy of $E_i = E_{i,0}/A$ each and can be treated as such mathematically.

Later, in chapter 4, we will introduce a tool which solves the cascade equation numerically in a very efficient way, allowing us to calculate particle fluxes fast.

2.4 Muon production

There are basically no muons entering earth as cosmic rays since they decay on the particles long journey through space. Thus all muons reaching ground are produced in atmospheric air showers. As already said in section 2.2, we distinguish between the conventional muon flux, dominating the low energy region, and the prompt flux which becomes important at about 10^5 to 10^6 GeV. Here we follow [Fed+15] and define a lepton as prompt if for its parent particle it holds that $c\tau < c\tau(K^0_S) = 2.68$ cm. By this definition the conventional flux consists of more muons than just those originating from the decay of $\pi^\pm$ and $K^\pm$ but as one can see from Figure 2.4 these make up by far the greatest fraction in the energy region where the conventional flux is important and in many cases to follow we will treat the conventional flux as consisting of just $\pi^\pm$ and $K^\pm$ induced muons.

All relevant decay channels for conventional muon production are presented e.g. in [Hon+95]. We only show the most important ones:

$$\begin{aligned} \pi^\pm &\to \mu^\pm \nu_\mu(\bar{\nu}_\mu) \qquad (\sim 100\%) \\ K^\pm &\to \mu^\pm \nu_\mu(\bar{\nu}_\mu) \qquad (63.5\%) \end{aligned} \tag{2.9}$$

And also one example of a by definition conventional contribution not from $\pi^\pm$ or $K^\pm$ decay:

$$K^0_S \to \pi^\pm \mu^\mp \nu_\mu(\bar{\nu}_\mu) \qquad (27\%)$$

It should of course be mentioned, too, that muons themselves might decay via:

$$\mu^\pm \to e^\pm \nu_e(\bar{\nu_e}) \bar{\nu_\mu}(\nu_\mu) \qquad (\sim 100\%).$$

Given in braces is the branching ratio for this particular decay channel.

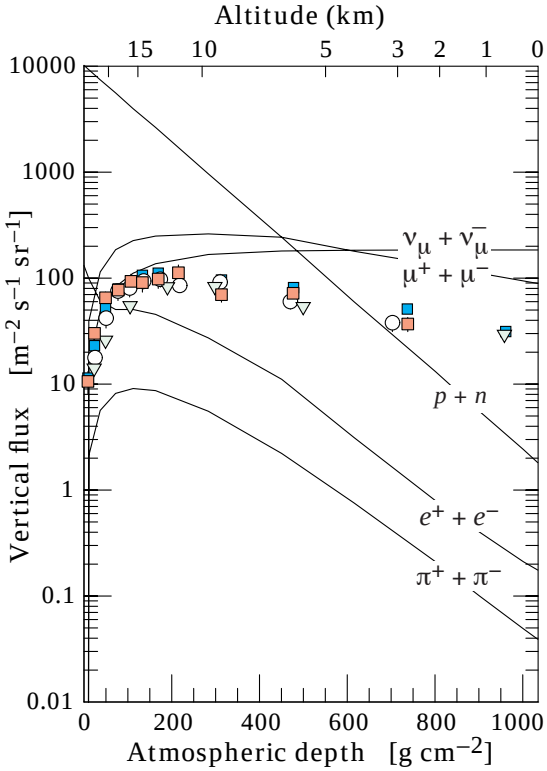

Figure 2.3: Estimated vertical fluxes of cosmic rays with $E > 1$ GeV. Figure taken from [PDG16].

The situation is not as easy for the prompt flux. First of all we have more different particles contributing, the most important ones being $D^{\pm}$, D^0, D_s, Λ_C and also unflavoured mesons like η. And all those have a variety of different decays channels which to list here is not seen as instructive. For details see [PDG+14].

Where in the atmosphere muons are produced is best describes in terms of the atmospheric slant depth given in Equation 2.4 which is the relevant parameter in the cascade equation. When a primary particle enters the atmosphere it does not instantly interact but will usually travel through some amount of matter as will the secondary particles before their interaction or decay. Figure 2.3 shows the typical depths at which muons and pions, the most important parent particle in the given energy region, are produced. The atmospheric depth at a certain height depends on the density above it. But this, the density profiles of the atmosphere, variates with time and location, making the muon flux at the detector variate over the year. That this is indeed the case has been known for over 70 years [For47; Bar+52] and the influence of atmospheric variations on air showers is measured to an ever higher accuracy by modern experiments like the Pierre Auger [Kei+04], IceCube [Roc09; Til+10; Des11; Gai], Daya Bay [An+18], and others. The to be expected variations for KM3NeT/ARCA are much lower than for these experi-

ments, especially IceCube, because KM3NeT/ARCA is located right in the subtropical zone [Klo16] where only weak variations are expected compared to the polar regions [Hon+15a]. The variation for different energies and zenith angles will be investigated and discussed in section 5.3.

Detailed and regularly improved calculations exist for the neutrino flux at low energies [Hon+95; Hon+17], commonly known as *Honda flux*, and also the prompt neutrino flux was calculated, where the *Enberg flux* [ERS08] established itself as the reference, but no similarly comprehensive attempts seem to have been made recently to calculate the muon flux. Thus we rely here on a calculation method to be introduced later in detail instead of the literature in order to give an detailed impression of the muon spectrum.

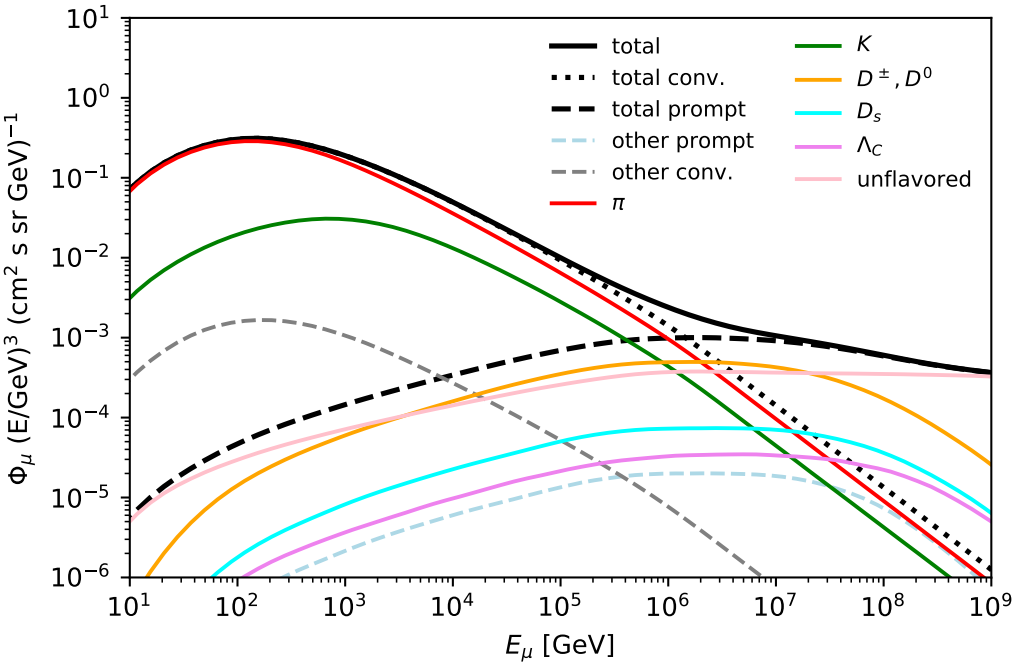

Figure 2.4: Partial contribution of parent particles to the flux of $\mu^{\pm}$ at a zenith angle of $\theta = 0°$. The calculation was done with MCEq [Fed+15], the US Standard Atmosphere [oa76] was used as atmospheric model, a simple broken power law model (TIG [TIG96]) as primary model and Sibyll 2.3c [Rie+17] as interaction model. Figure taken from [Fed+15] with slight modifications.

Figure 2.4 shows an exemplary muon spectrum at sea level calculated from a simple broken power-law primary spectrum and scaled by E^3 in order to make more details visible. The first thing to notice is that the flux becomes lower at higher energies (the dip at low energies is caused by the scaling) which is unsurprising since we find the same general behaviour in the primary flux which starts the muon production in the first place.

The for this work most important thing to notice are the dotted and the dashed black lines, representing the total conventional and total prompt flux respectively. At low energies the conventional flux makes up for by far the largest fractions of muons but around 10^6 GeV the prompt flux becomes equally important and then dominates the spectrum at very high energies. Why is that? The answer lies in the definition: conventional particles have a relatively long lifetimes, $2.6 \cdot 10^{-8}$ s for $\pi^{\pm}$ and $1.2 \cdot 10^{-8}$ s for $K^{\pm}$, whereas the lifetimes of prompt particles are much shorter, e.g. 10^{-12} s for $D^{\pm}$ (all numbers from [PDG+14]). This makes an important difference because when parent particles travel through the atmosphere they might – as can be seen from Equation 2.3 – either decay, producing muons, or interact again, thus not contributing to the muon flux. And the higher the particles' energy, the longer their lifetimes, the lower the probability of decay compared to interaction which causes a steepening in the conventional muon spectrum of approximately one order of magnitude compared to the primary spectrum [GER16]. Prompt particles, since they are heavier, are fewer in number and thus do not play a role at low energies but since the conventional spectrum falls steeply they become important at some point as we have seen. Of course they are in principle subject to the same processes and might also interact instead of decay but their much shorter lifetimes favour decay up to much higher energies compared to pions and kaons. This can be quantified.

We introduce the critical energy E_{crit} which is the energy below which interaction and above which decay is more probable. It can be calculated by the following formula [Gai13]:

$$E_{crit} = \frac{\epsilon_P}{\cos\theta^*} = \frac{m_P c^2 h_0}{c\tau_P} \tag{2.10}$$

where P stands for the parent particle, m_P and τ_P for its mass and lifetime respectively, h_0 for the scale height of the atmosphere and θ is the zenith angle (which needs to be corrected for large angles in order to account for the earth's curvature). Table 2.1 gives the values of ϵ_P for vertically entering particles for the different atmospheric models that are used by the KM3NeT collaboration or in this work. The *KM3NeT Standard* atmosphere is used for most calculation and will serve us here as a reference as well. It will be explained in detail later in this work, as will be the other models.

Particle	KM3NeT Std	MSIS-00 Jan	MSIS-00 July	CKA Win	CKA Sum
$\pi^{\pm}$	167	168	172	167	172
$K^{\pm}$	1238	1242	1269	1238	1268
$D^{\pm}$	$436 \cdot 10^5$	$438 \cdot 10^5$	$448 \cdot 10^5$	$437 \cdot 10^5$	$448 \cdot 10^5$

Table 2.1: Critical energy in GeV for different atmospheres for $\theta = 0°$. Except for the first, these are atmospheres explicitly modelled for the position of the KM3NeT/ARCA detector.

This competition between interaction and decay of parent particles is essential in understanding the muon flux components and we will meet it time and again.

Since the reader might more familiar with atmospheric neutrino rather than muon

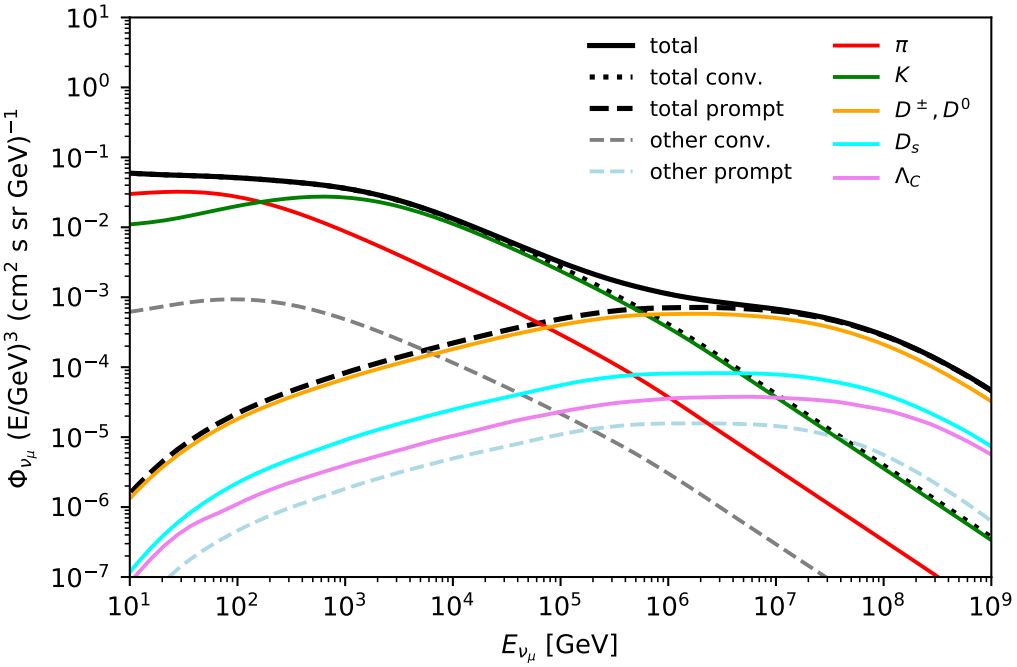

Figure 2.5: Partial contribution of parent particles to the flux of $\nu_\mu + \bar{\nu_\mu}$ at a zenith angle of $\theta = 0°$. The calculation was done with MCEq [Fed+15], the US Standard Atmosphere [oa76] was used as atmospheric model, a simple broken power law model (TIG [TIG96]) as primary model and Sibyll 2.3c [Rie+17] as interaction model. Figure taken from [Fed+15] with slight modifications.

fluxes Figure 2.5 show the neutrino flux calculated under the same model assumptions as the muon flux in Figure 2.4 for comparison and we want to point out two important differences here.

The first is that for muons the contribution from pions is always larger than from kaons but for muon neutrinos this is different except for low energies. When just looking at the decay channels 2.9 this might seem strange because are produced together. The reason for the difference is that in a pion decay most energy is carried away by the muon whereas in the kaon decay the energy is split almost equally [FTD12].

The second difference is that for neutrinos the prompt flux comes to the largest part from D mesons and a few heavier ones, whereas for the muon prompt flux unflavoured mesons, especially η, play a very important part. The η mesons can decay electromagnetically and thus only muons and no neutrinos are produced. Admittedly, the branching ratio of η to muons is suppressed but they are more abundant in air showers than charmed mesons and thus play an important role [IMM09]. For these two reasons there is no simple correlation between the atmospheric muon and muon neutrino flux as one might

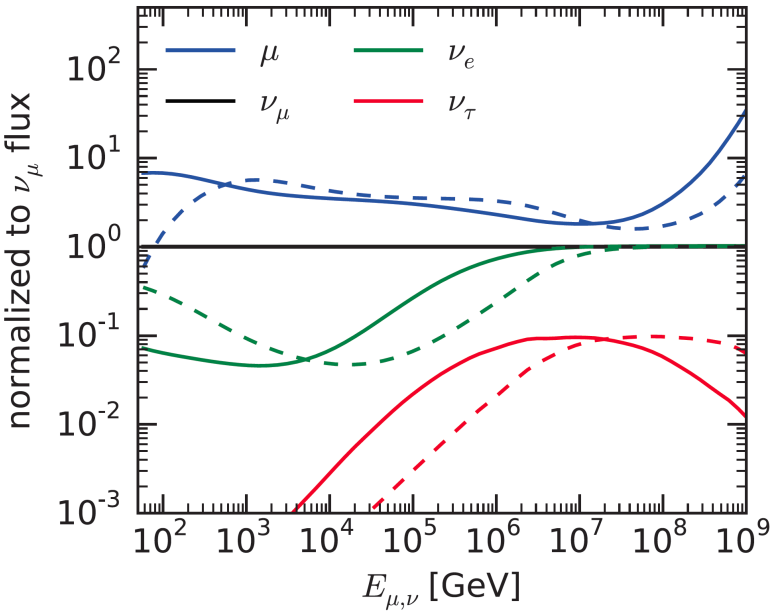

Figure 2.6: Flavour ratios of leptons at the surface, normalised to the muon neutrino flux. The calculation was performed using the H3a primary flux model and SIBYLL 2.3 as interaction model for $\theta = 0°$ (solid) and $\theta = 90°$ (dashed). Figure taken from [Fed+15]

otherwise would have guessed. Figure 2.6 shows a comparison.

2.5 Muon energy loss

When charged particles propagate through media such as air or water they lose energy. We focus here on muons because they are the only charged particles whose propagation down to the detector is of interest for us and the energy losses of parent particles in the atmosphere during the muon production process are almost negligible ($\lesssim$ 1 GeV) [PDG16].

Figure 2.7 gives an overview of different muon energy loss regions per column depth over of the muon momentum. In the relevant energy region above 30 GeV energy and moment are almost the same up to the factor of c (for comparison: $m_\mu = 106$ MeV [PDG+14]) and we therefore do not make a distinction here or anywhere else in this work and only talk of energy. In that region the energy loss can be well described through the stopping power

$$\left\langle -\frac{\mathrm{d}E}{\mathrm{d}X} \right\rangle = a(E) + b(E)E \tag{2.11}$$

where X is the atmospheric slant depth and defined as in Equation 2.4. The term $a(E)$

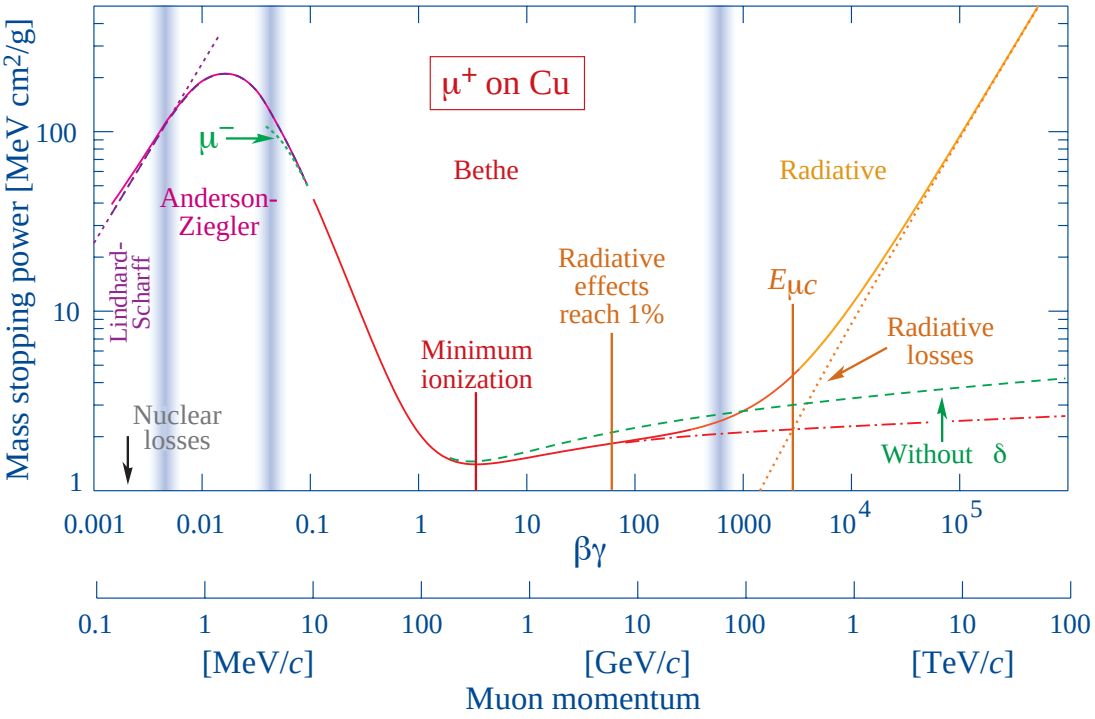

Figure 2.7: Stopping power $\langle -\mathrm{d}E/\mathrm{d}X \rangle$ for μ^+ in copper as function of the muon momentum. Figure taken from [PDG16].

contains electronic losses by ionisation and $b(E)$ represents radiative losses which are mainly bremsstrahlung, pair production and photonuclear interactions,

$$b = b_{\text{brems}} + b_{\text{pair}} + b_{\text{nucl}}.$$

The effect of this energy loss can be seen in Figure 2.8 which shows the muon intensity over the depth. This curve has been constructed from the measurement of various experiments where the overburden at each detector for the different zenith angles has been taken into account. The shaded areas represent neutrino induced muons and one can see that at slant depths above 10^6 g/cm^2, i.e. large zenith angles at the KM3NeT detector, their contribution should not be neglected.

We will not carry out any calculations ourselves but instead rely on tabulated data. The next few paragraphs are just to give a rough impression of the different processes involved.

The **electronic stopping** power (ionisation) $a(E)$ can be calculated with the Bethe-Bloch equation which contains contribution from all inelastic scatterings and some cor-

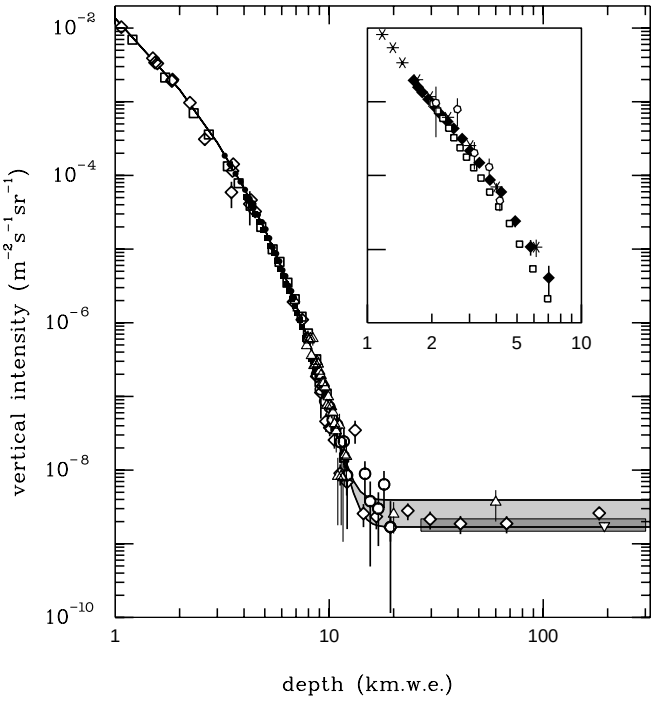

Figure 2.8: Vertical muon intensity over depth with measurements from various experiments. ♢: Crouch, □: Baksan, ○: LVD, ■: Frejus, △: SNO. The brighter shaded area represents neutrino induced muons above a 2 GeV energy threshold where the upper line is for horizontally induced and the lower line for vertically upward moving ones. Figure taken from [PDG16]; references for the experimental data are given there.

rections:

$$a(E) = K\frac{Z}{A}\frac{1}{\beta}\left[\frac{1}{2}\ln\frac{2m_e c^2\beta^2\gamma^2 Q_{\max}}{I^2} - \beta^2 - \frac{\delta}{2} + \frac{1}{8}\frac{Q_{\max}^2}{(\gamma Mc^2)^2}\right] + \Delta\left|\frac{\mathrm{d}E}{\mathrm{d}X}\right|. \tag{2.12}$$

Here Q is the kinetic energy of the scattered electron, I the mean excitation potential of the material and the final summand is a correction that takes bremsstrahlung of electrons into account and is given by:

$$\Delta\left|\frac{\mathrm{d}E}{\mathrm{d}X}\right| = \frac{K}{4\pi}\frac{Z}{A}\alpha\left[\ln\frac{2E}{m_\mu c^2} - \frac{1}{3}\ln\frac{2Q_{\max}}{m_e c^2}\right]\ln^2\frac{2Q_{\max}}{m_e c^2}. \tag{2.13}$$

Bremsstrahlung is caused when a charged particle is accelerated in the coulomb field of another particle and it is in principle similar to synchrotron radiation. Different from electrons bremsstrahlung is for muons not the main radiative energy loss because it is suppressed by a factor of $(m_e/m_\mu)^2 = 2.3 \cdot 10^{-5}$. One needs to calculate the differential

cross sections for muon bremsstrahlung from a screened nucleon and from the atomic electrons and then integrate over the sum of these. For details see [GMS01].

Electromagnetic interaction of a high energy muon with a nucleus might lead to **direct pair production** of an e^+e^- pair which is the most important energy loss process for muons. There are different approaches on how to calculate the cross section and for the tabulated data that are later used to calculate the energy loss in air, the semi-analytical approach by Kokuoulin et. al. [KP71] was used.

A **photonuclear interaction**, also called hadroproduction, is an electromagnetic muon-nucleon scattering process in which, as the alternative name suggests, hadrons are produced.

In the next chapter *MCEq*, the tool of our choice for the calculation of lepton fluxes, will be introduced and for this the developer has calculated and tabulated his own values for the muon energy loss in air und the procedure can be found here [Gar16]. The original version of MCEq was extended to allow for muon propagation through water and for this tabulated data from the Particle Data Group* were used and extrapolated to higher energies. In the energy region where the extrapolation was necessary $a(E)$ does not play a role any more and $b(E)$, though in principle still a function of E, varies hardly [GER16].

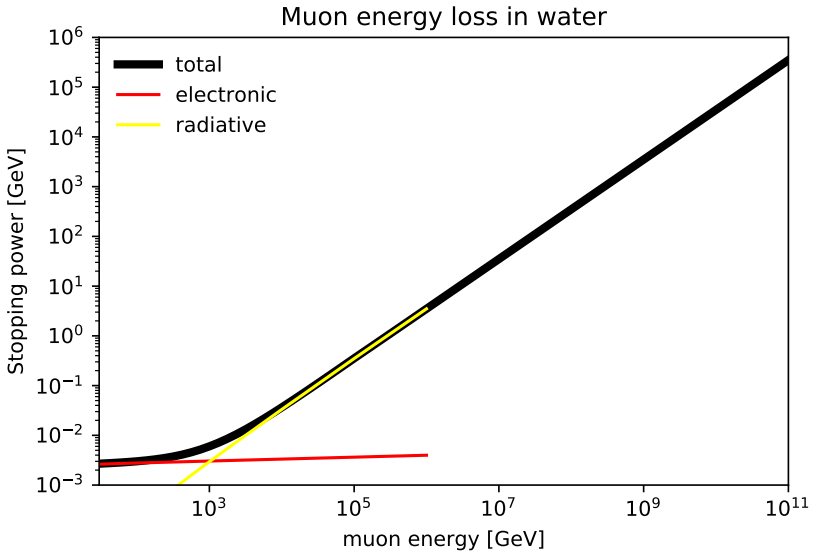

Figure 2.9: Stopping power $\langle -\mathrm{d}E/\mathrm{d}X \rangle$ for $\mu^{\pm}$ in water as function of the muon energy. Data were only tabulated up to 10^6 GeV (see range of the yellow and red line), for higher energies a simple linear extrapolation was used.

*http://pdg.lbl.gov/2017/AtomicNuclearProperties/MUE/muE_water_liquid.txt

Chapter 3

The KM3NeT/ARCA neutrino telescope

In this chapter some information about the KM3NeT/ARCA detector is presented. Since for this work only the size, position and some error estimates are relevant, it will be kept brief. Detailed information on the whole KM3NeT project can be found in [AM+16].

KM3NeT is an extensive research infrastructure in the Mediterranean deep sea which is currently under construction. It is more or less the successor of ANTARES [Age+11] where many lessons for such a type of detector could be learnt. KM3NeT/ARCA is the part dedicated to the study of high-energy cosmic neutrinos and is about to get build at the KM3NeT-Italy site off the coast of Sicily. The other part of the experiment, KM3NeT/ORCA, whose future home is off the coast of France, is supposed to determine the neutrino mass hierarchy one day.

KM3NeT is a Cherenkov telescope, meaning it gets its data by the collection of Cherenkov light. That is emitted if a charged particle moves faster in a medium than the speed of light is in that medium. When it can be assumed that the particles travel with almost the speed of light as is usually the case in situations considered here, the angle at which the light is emitted depends on the surrounding medium only. Since light gets emitted in all directions at this angle, a characteristic cone is formed from measurements of which the direction of the incident particle can be reconstructed.

For the measurement of the Cherenkov light so called **D**igital **O**ptical **M**odules (DOMs) are used which are glass spheres, hosting 31 photo-multiplier tubes (PMTs) and their associated readout electronics. 18 DOMs are attached to a detection string (which is actually two strings) with a spacing of 36m. These strings are attached to the sea floor. Figure 3.1 shows a picture of one such DOM and also a model of a detection string.

One ARCA building block consists of 115 strings with an average spacing of 90m. The layout is depicted in Figure 3.2. As can be seen from there, a building block is approximately cylindric with a radius of 500m and a height of 612m. This means the volume of one building block is approximately 0.48 km^3, thus almost 1 km^3 for two building blocks, hence the name KM3NeT: Cubic Kilometre Neutrino Telescope. The bottom of such a building block lies 3420m below sea level. When in later chapters it is written of the muon flux at or through the detector, the flux entering two of these building

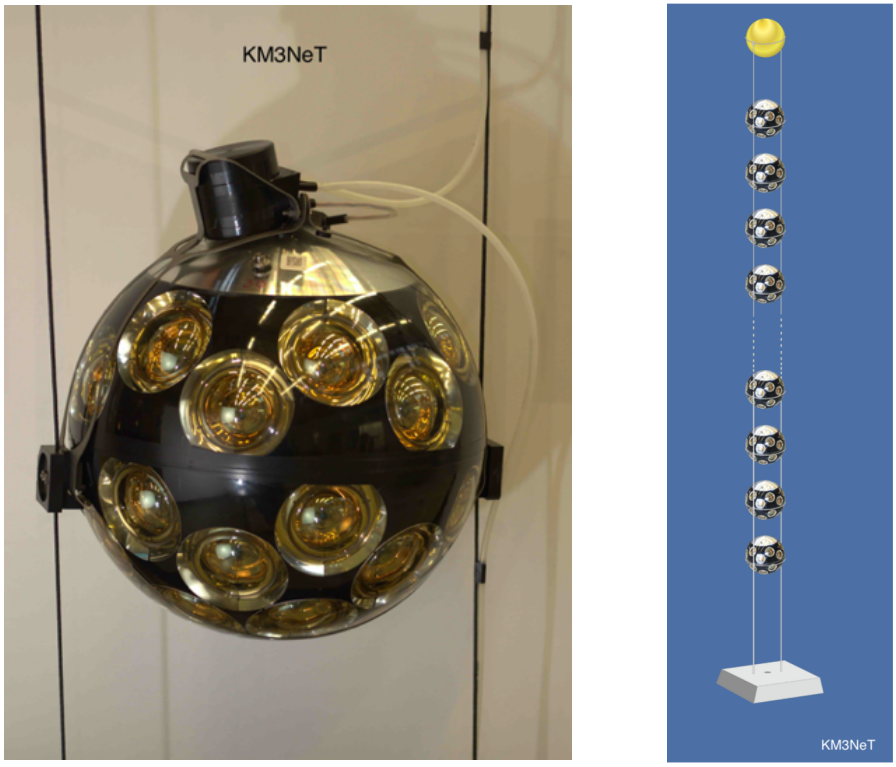

Figure 3.1: Left: The KM3NeT digital optical module (DOM); right: a detection string which hosts 18 DOMs (36m spacing). Figures taken from [AM+16].

blocks is meant, reduced by a small factor because they are build closely together as can be seen on the right in Figure 3.2 and some muons might be counted twice.
There is one exception to this: For the CORSIKA production and the further processing thereof a different volume was chosen, called the *can*. This is the instrumented volume extended by three times the absorption length of light in water because the signal of particles closely passing by should be investigated as well. This *can* with its bottom at 3500m below sea level has a radius of 705m and a height of 920m. When the comparison is made between CORSIKA and MCEQ in subsection 4.5.2 the *can* volume will also be used for the latter in that one case.

Figure 3.3 shows the position of the KM3NeT-Italy site off the coast of Sicily at 36°16' N 16°06' E where the ARCA detector will take data at some time in the future. The position is relevant for the simulations because it determines the atmospheric density profile. It would also be relevant if geomagnetic effects had to be taken into account but these are not important in the energy region relevant in this work as was discussed in section 2.1. The position also tells us that ARCA is right inside the subtropical zone [Klo16] which means that seasonal variations will be small.

One last thing important for this work is an error estimate for the reconstructed energy. An fluctuation of 10% on the absorption and scattering of light, which is the order of

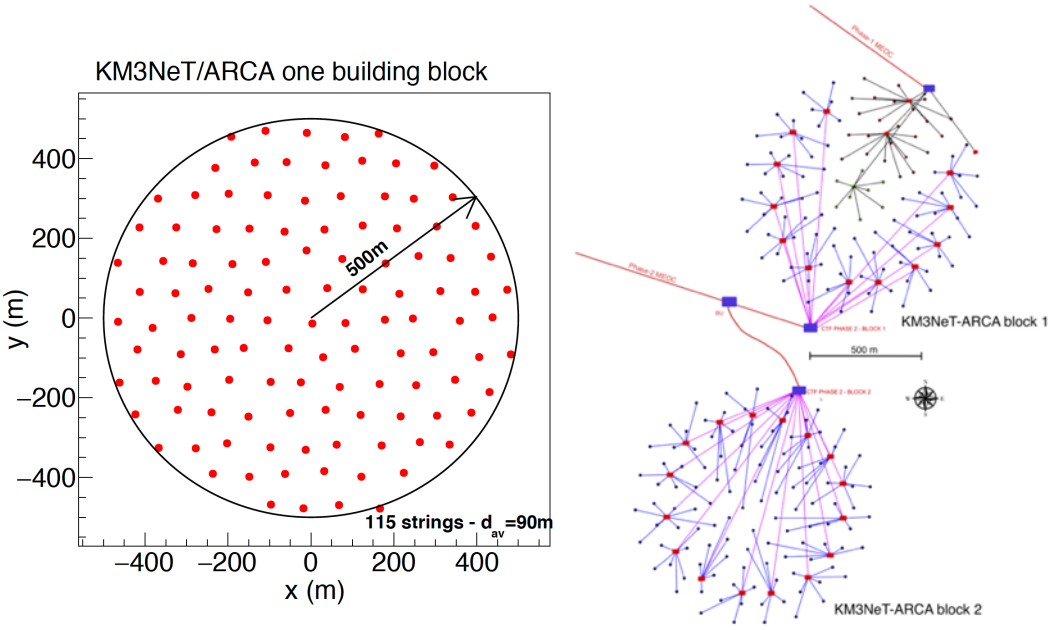

Figure 3.2: Left: The footprint of one ARCA building block (top view), with 115 strings (90 m average spacing). The instrumented volume is 0.48 km^3 (R = 500 m, z = 612 m). Right: Layout of the two ARCA building blocks which are planned to get build on phase 2.0. Figures taken from [AM+16].

accuracy ot the measurements, has been found to lead to a relative error $\Delta E/E$ of 8% and 0.6% respectively. Another error of 5% comes in if one assumes an uncertainty of 10% on the effective area of the PMTs. The by far largest error comes from the energy reconstruction procedure and is $\backsimeq 0.27$ in units of $\log_{10}(E_\mu)$, see Figure 3.4.

Figure 3.3: Position of the KM3NeT/ARCA detector in the Mediterranean. The yellow line indicates the cable. Figure taken from [AM+16].

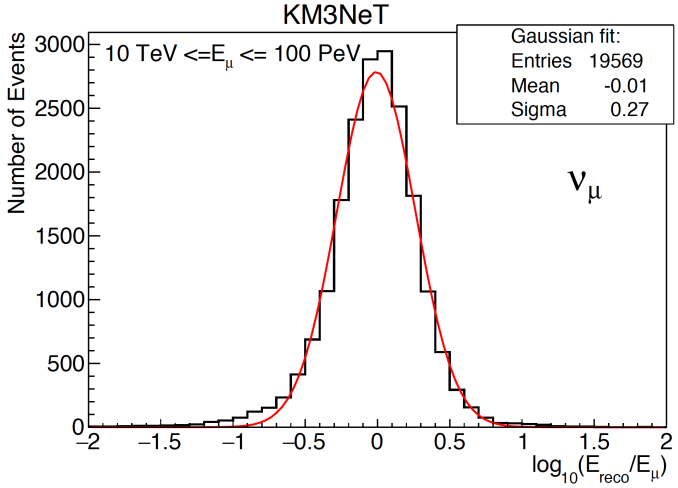

Figure 3.4: Distribution of the reconstructed divided by the true muon energy in logarithmic space for events with $E \geq 10$ TeV that satisfy a containment criterion. The red line represents the Gaussian fit. Figure taken from [AM+16].

Chapter 4

Simulating the muon flux

It is important for experiments like KM3NeT to accurately simulate the different lepton fluxes that reach the detector in order to disentangle measurements properly and test or train the software supposed to analyse events. And in our case, simulations are the only thing we can work with since the detector is not build yet and thus there are no measurement data available.

Nowadays there are different options when one wants to calculate lepton fluxes. The classical approach is to run a full scale Monte Carlo simulation of the atmospheric showers which outputs single events that can then be used for further processing in the detector simulation chain. The disadvantage is that this requires large computing powers, is very time consuming, and has large statistical errors due to weighting until the production becomes very large which it not yet is for KM3NeT. Since we ware only interested in the fluxes here we can rely on a different approach and numerically solve the cascade equation, using the **M**atrix **C**ascade **Eq**uation Solver MCEq.

At the beginning of this chapter we will discuss different models of the cosmic ray flux, the atmosphere, and nuclear interactions (event generators) which both approaches described above need as input. Then Corsika, a commonly used software for Monte Carlo air shower simulations, will be introduced as will MCEq and the chapter closes with a comparison of the outputs.

4.1 Cosmic ray flux models

When one wants to calculate lepton fluxes from atmospheric showers, a model of the primary cosmic ray flux (which starts the atmospheric showers it the first place) is needed. In Corsika this models enters when events are weighted from the production spectrum to a model, in MCEq the flux model directly serves as a boundary condition for the cascade equation.

There is a variety of primary flux models around and we will introduce three of them. One very simple one which will be used mainly for comparisons and two more sophis-

ticated ones in the choice of which we follow T. Heid who already investigated lepton fluxes at the KM3NeT/ARCA detector [Hei17]. All these models are motivated by theoretical considerations about the sources and then fit to data and their complexity is limited. There is also an approach to a completely data-driven model, the Global Spline Fit (GSF), [Dem+17] that looks very promising. Unfortunately, the data tables were not yet made publicly available by the time of writing of this thesis but it is certainly something worth looking at in future analyses.

The first model by M. Thunman, G. Ingelman, and P. Gondolo (**TIG**) is a simple broken power law model [TIG96]. It contains only protons with a flux of

$$\begin{aligned} 1.7 \cdot 10^4 (E/\mathrm{GeV})^{-2.7} \frac{\text{protons}}{\mathrm{m}^2 \text{ s sr GeV}} \qquad & \text{for } E < 5 \cdot 10^6 \text{ GeV} \\ 174 \cdot 10^4 (E/\mathrm{GeV})^{-3} \frac{\text{protons}}{\mathrm{m}^2 \text{ s sr GeV}} \qquad & \text{for } E \geq 5 \cdot 10^6 \text{ GeV}. \end{aligned} \tag{4.1}$$

It is certainly too primitive to accurately describe the primary flux but in gives some orientation when comparing models and also helps to make features in lepton fluxes at high energies more visible when the exact values are not so important like e.g. in Figure 2.4.

The second, a more sophisticated, model is the **Hillas-Gaisser model** which is based on Hillas ideas [Hil06], fit to data by Gaisser [Gai12]. Like for many other models, the underlying assumption here is that there are three populations of cosmic rays which is the minimal requirement to model the most distinct features, i.e. the knee and ankle, of the spectrum. The first population is usually associated with particles accelerated by supernova remnants where a rigidity-dependent cutoff leads to the knee. The second population, called "Component B" by Hillas, accounting for the flux between the knee and the ankle, is also assumed to originate in our galaxy but the source remains subject to debate. The third, highest energy, population is assumed to be of extragalactic origin. Some details about speculative sources were already discussed in section 2.1.

The particles are conventionally grouped in five mass groups which are H, He, CNO, Mg-Si, and Mn-Fe to which relative abundances and cutoffs, roughly according to Equation 2.2, are assigned. The flux of one such group i is then described by the following formula:

$$\phi_i = \sum_{j=1}^{3} a_{i,j} E^{-\gamma_{i,j}} \cdot \exp\left[-\frac{R}{Z_i R_{c,j}}\right]. \tag{4.2}$$

Here j stands for the population, a is the corresponding normalisation and γ is the spectral index and the exponential factor at the end represents the rigidity-cutoff. Values for the first population are derived from direct results of CREAM [Ahn+10] and then extrapolated to a rigidity around 4 PV whereas for the second indirect all-particle data had to be used up to the cutoff at 30 PV. There are two different approaches to describe the third population: either as a mixed composition (**H3a**) with a cutoff at 2 EV or protons only (**H4a**) with a cutoff at 60 EV. How well this model fits to data can be seen in Figure 4.1.

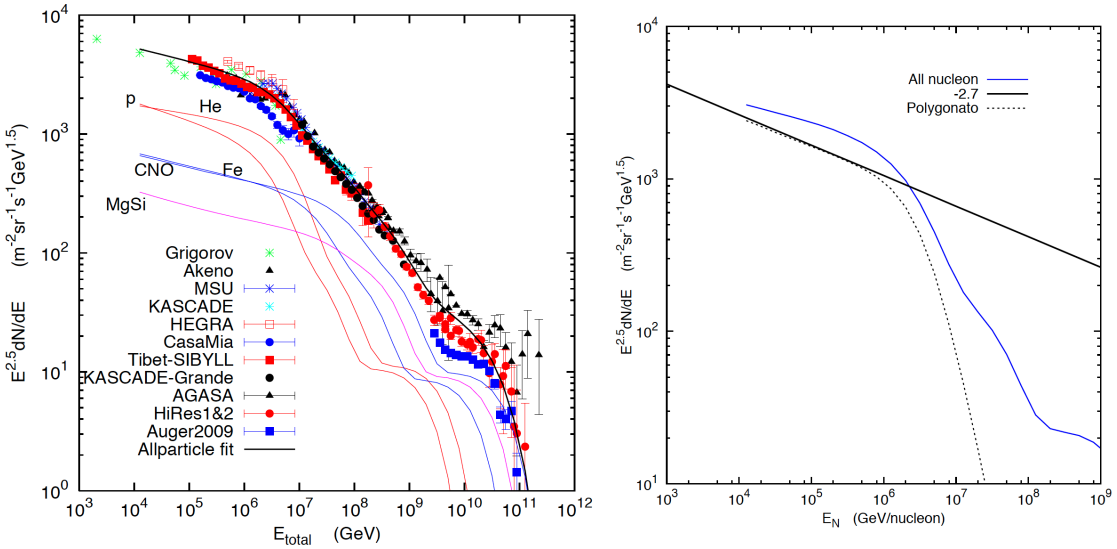

Figure 4.1: Left: The Hillas-Gaisser model (H3a) compared to data from different experiments. Right: The model compared to other very primitive model, a simple $E^{-2.7}$ differential spectrum and the Polygonato model which models only the galactic component. Figure taken from [Gai12].

The third model to be introduced here is the **Gaisser-Stanev-Tilav model** [GS13]. Its way of modelling is the same as for the Hillas-Gaisser model but cutoffs and thus fitting parameters turn out different. It also comes in two version, **GST3** and **GST4**, of which the latter has an additional fourth population.

The rigidity cutoff of the first population comes much earlier at 120 TV because significantly harder spectra are assumed from newer data [Adr+11]. The second population gets cut off at 4 PV, the value for the first population in the Hillas-Gaisser models. The third generation's cutoff is at 1.3 EV for the three and at 1.5 EV for four generation model which has its last cutoff at 40 EV. The first and second population for which direct measurement data are available consist of all groups of nuclei we defined above. The third population is in this model only composed of protons and iron. A fit of the 3-gen model to data can be seen in Figure 4.2a. As one can see match is quite good. But it has a flaw: it is only good in regard to energy. If one looks at the composition it does not fit at all as can be seen from Figure 4.2b and this is the reason why the 4-gen model was thought up.

A computational implementation of all the flux models discussed above and more was compiled by A. Fedynitch at. al. for their publication [FTD12] and is available freely on GitHub*. It is also directly implemented in MCEq. Figure 4.3 shows a comparison of the different models.

*`https://github.com/afedynitch/CRFluxModels`

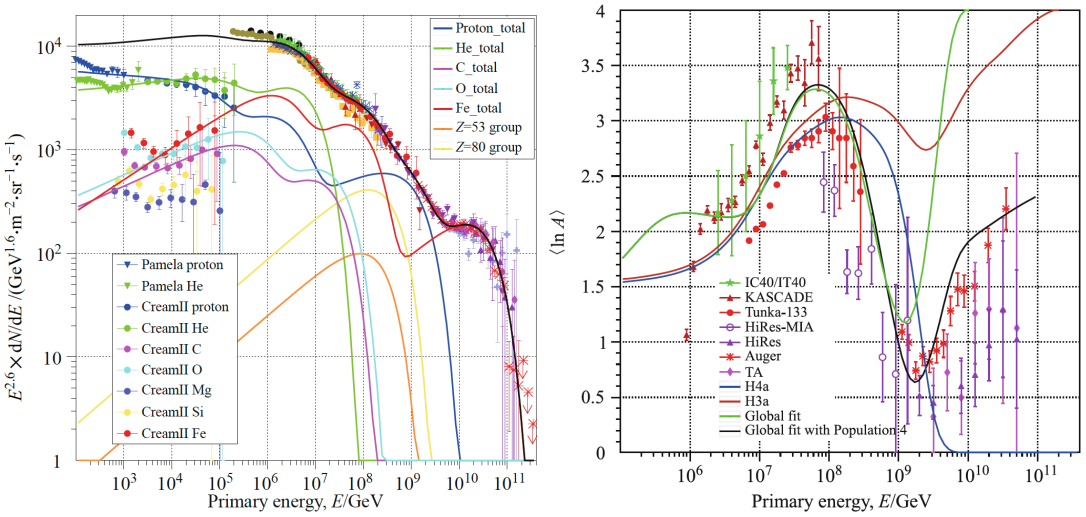

(a) Overview of the spectrum with data from different experiments and the GST3 model fit into it. The coloured lines show individual groups of nuclei from all populations.

(b) Mean ln$A$ for the two different models with their two sub-models introduced in this section.

Figure 4.2: The Gaisser-Stanev-Tilav model compared to data from different experiments. Many of the air shower data were shifted by some constant value in order to make them compatible to one another. Values for this can be found in the publication. Figures taken from [GS13].

4.2 Models of the atmosphere

As discussed in section 2.4 the muon flux depends on the slant depth and thus should depend on the atmospheric profile. In many calculations of lepton fluxes like the early ones of Honda [Hon+95] the *US Standard atmospheric model (US-Std)* [oa76] from 1976 is used which has established itself as a reference model. But since the KM3NeT/ARCA detector's location is in a different climate zone and we also want to study seasonal variations we need a model better fitted to our purposes. This will be the *NRLMSISE-00* [Pic+02] model which is integrated in MCEq and can also be used as a basis for deducing an atmospheric model that can be used by Cosika.

4.2.1 The NRLMSISE-00 atmospheric model

NRLMSISE-00 is an empirical model of the earth's atmosphere and a freely available software can calculate a density and composition profile for a specified location and day of the year. As explained at [Msia], *NRL* in the abbreviation stand for the US Naval Research Laboratory which publishes the data, *MSIS* stands for mass spectrometer and incoherent scatter radar which are the two primary data sources used in earlier versions of the model, *E* indicates the extension of the model to the exosphere and *00* stands

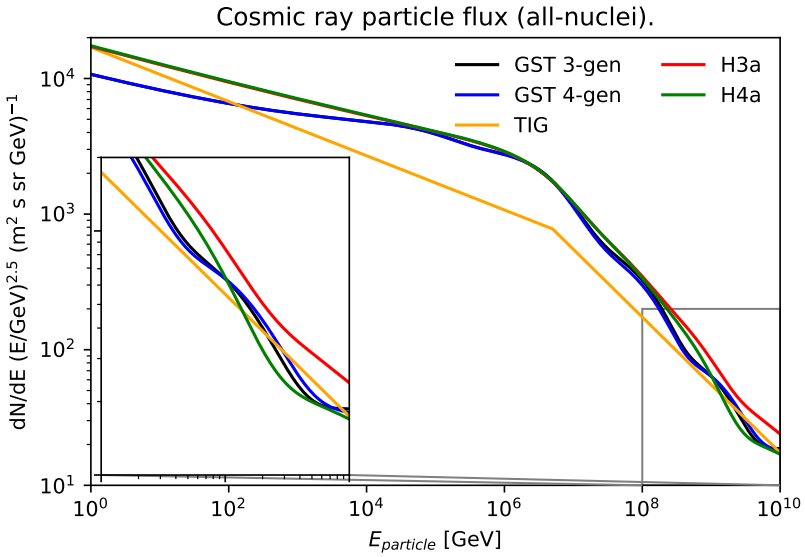

Figure 4.3: Comparison of the all-particle spectrum of all the models discussed above.

for the year of the release. NRLMSISE-00 is based on the MSISE90 model but now extensively uses satellite data. Information how data were acquired in the earlier models (except from what the model's name already tells) can be found at [Msib]. In the version used here we specify the day of the year but not the year itself and in return get an average profile for that day.

Figure 4.4 shows the density profile above the ARCA site derived from NRLMSISE-00 data. What is plotted here and in all other plots that show data for a certain month are the data for the first day of that month. As one can see the density falls approximately exponentially and does not vary too much on the grand scale. But variations there are and to make them better visible Figure 4.5 shows the density of the respective month relative to that in January.

As can be seen there, one cannot generally say that the atmosphere is less dense on a representative warm summer day than a cold winter day because the atmospheric layers behave quite differently and temperatures at some height do not necessarily correlate with temperatures at sea level, but the part of the atmosphere relevant for muon production is indeed less dense in summer than winter which will be discussed in section 5.3. On the right side of Figure 4.5 one finds that at low heights the atmosphere is most dense in January which is just as expected since then it is coldest in the troposphere. The lowest density can, unsurprisingly, be found in July and August when it is hot and the atmosphere, at least the tropospheric layer, expands.

As discussed in section 2.4 not the density but the atmospheric depth is the quantity most important for muon production. Thus Figure 4.6 shows on the left the variation thereof which of course has features similar to the density variation's since the depth is an integration over the density, see Equation 2.4. The relation is approximately linear

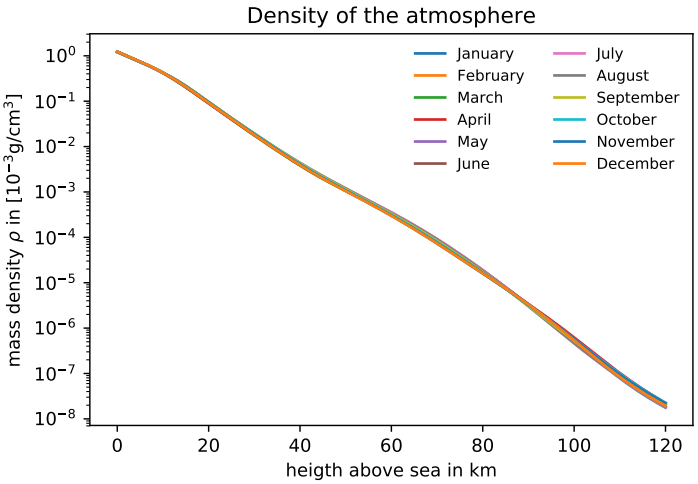

Figure 4.4: Density profile of the atmosphere at the KM3NeT/ARCA site derived from NRLMSISE-00 data. Figure adopted from [Hei17].

but not exactly and is shown on the right of Figure 4.6. The steepness for the summer months is a little lower than for the winter months which results in the seasonal variations. A better resolved plot and a detailed discussion on this will be given in section 5.3.

4.2.2 CORSIKA's atmospheric model

Unfortunately the NRLMSISE-00 model cannot be directly employed in the CORSIKA simulation software. The atmospheric models used there always consist of five layers, whereof the lower four layers are described by an exponential function of height h for the atmospheric depth X

$$X(h) = a_i + b_i e^{-h/c_i}, \qquad i = 1, \ldots, 4 \tag{4.3}$$

and the fifth layer, the highest, decreases linearly

$$X(h) = a_5 - b_5 \frac{h}{c_5}. \tag{4.4}$$

The parameters a_i, b_i, and c_i have to be fitted and e.g. to the NRLMSISE-00 model. That it makes sense to model the atmosphere in exponential layers can be seen from Figure 4.4; the fifth layer usually starts where densities are already so low that the behaviour of the profile does not make much of a difference. For details on how the CORSIKA model can be fit to data see [Hei17]. The parameters for the KM3NeT-Std atmosphere that was used for the CORSIKA production run so far and which we will use occasionally are given in Table 4.1.

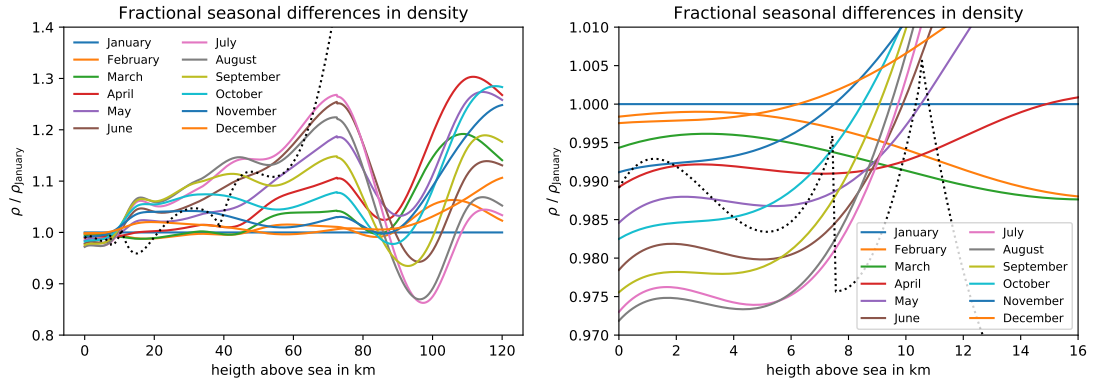

Figure 4.5: Density variations of the atmosphere at the KM3NeT/ARCA site. NRLMSISE-00 data for the respective month are shown relative to January. The figure on the right is a more detailed view of the lower atmosphere. The dotted black line marks the KM3NeT Std atmosphere for comparison. Figure adopted from [Hei17].

Layer	1	2	3	4	5
a_i	-160.62	-94.2	0.8116	-6.9957	0.0144
b_i	1198.62	1151.43	1319.63	449.65	
c_i	977647.64	878153.55	636143.04	811710.06	748872601
$h_{\max}$ [cm]	$7.5 \cdot 10^5$	$10.5 \cdot 10^5$	$38.5 \cdot 10^5$	$10.5 \cdot 10^6$	

Table 4.1: Parameters for the KM3NeT-Std atmosphere

Corsika and MCEq both assume, somewhat unphysically, there to be no variations in the atmospheric composition – neither in with height nor with location or time. In CORSIKA the atmosphere is assumed to consist of 78.1% N_2, 21.0% O_2, and 0.9% Ar. MCEq assumes an average mass of a target nucleus of 14.5 g/mol (where here all nucleons are seen as separate in the definition of mol) which is essentially the same thing.

4.3 Interaction models

The third important ingredient one needs to calculate lepton fluxes – besides a model for the primary flux and one for the atmosphere – is an interaction model, also called an event generator, which describes what happens when a cosmic ray nucleus interacts with an air nucleus. Since the dominant interactions are QCD processes and the running coupling constant is too large in most cases, ordinary perturbation theory cannot be applied and usually phenomenological approaches are used to describe the interactions. For the Corsika production run so far Sibyll 2.3 [Rie+15b; Rie+15a] was used as interaction model. MCEq also supports that versions of Sibyll as well as the legacy version 2.1 [Ahn+09] and the newest version 2.3c [Rie+17]. Other supported models are

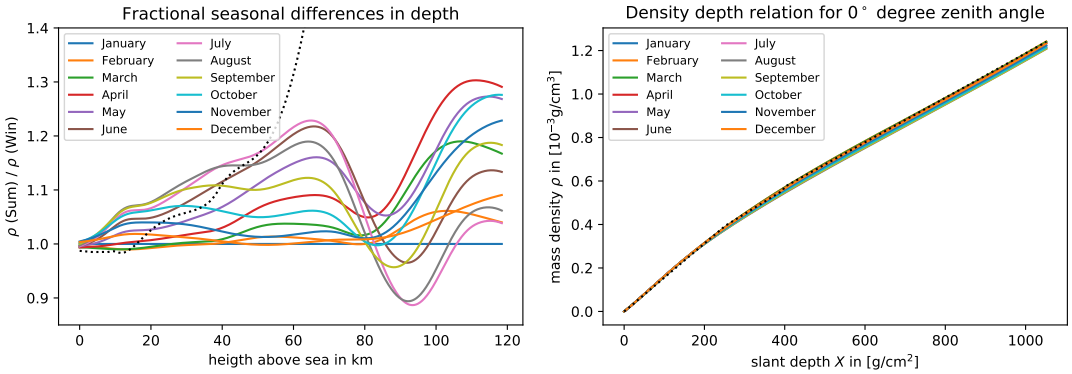

Figure 4.6: Left: Depth variations of the atmosphere at the KM3NeT/ARCA site. NRLMSISE-00 data for the respective month are shown relative to January. Right: Density depth relationship. The dotted black line marks the KM3NeT Std atmosphere for comparison. Figures adopted from [Hei17] and [Fed+15].

two recent versions, 03 and 04, of QGSJET-II [Ost11] and the older version QGSJET 01C [KOP97], EPOS-LHC [Pie+15], and DPMJET-III [RER01] and a revised version thereof [FE15]. Even though there is this variety of models available we mostly have to rely on SIBYLL. The other models rule themselves out for different reasons in most cases but will still be of use to us for error estimates or as low energy extension. In the next few paragraphs we will briefly discuss the models and their deficits. A more thorough discussion of this topic can be found in [FTD12] and parts of the following paragraphs are written closely to that publication.

SIBYLL is the least sophisticated of the models discussed here but nevertheless quite successful. This is because it is explicitly designed for air shower simulations which means its puts a focus on the energy flow and particle production in the forward phase space region and implements extrapolation algorithms for predictions at very high energies. For interactions in the soft phase space region Sibyll employs the Dual Parton Model [Cap+94] which is just a particular implementation of Gribov's Reggeon calculus [Gri68] and also the basis of the DPMJET models discussed below. For the hard pertubative component SIBYLL uses a minijet model which allows for extrapolation to the ultra-high energy region without many parameters, an important part in the model's success in air shower calculations. Version 2.3 was released in 2016 and was tuned to LHC data from fixed-target experiments like TOTEM [Ane+08]. Also since that version the production of hadrons containing charm quarks is supported which is of the utmost importance for the investigation of the prompt muon flux discussed in this thesis. A detailed introduction to Sibyll, including a description of the evolution of the model, can be found in [Eng+17]. Only minor changes, e.g. a lower K^+ production, were introduced in version 2.3c and the prediction for extensive air showers are very similar to those of SIBYLL 2.3.

QGSJET, which stands for **Q**uark-**G**luon-**S**tring model with mini**jet** production, is also a phenomenological model based on Gribov's Reggeon calculus for the description

of nuclear and hadronic collisions. Like Sibyll it was also explicitly optimised for the simulation of air showers with special emphasis on the extrapolation to ultra-high energies. The newest version, QGSJET-II-04, is tuned to recent LHC data which is the only real difference to the earlier version QGSJET-II-03 and we will thus use only version 04 here. Unfortunately, all QGSJET-II versions share a large deficit: they do not support the production of hadrons containing a charm quark. Since these hadrons make an important contribution to the prompt flux, see Figure 2.4, QGSJET-II cannot be used for most analyses in this work. It will be employed though to get an error estimate on the conventional flux.
The older version, QJSJET 01C, is mentioned here because it actually does support charm production. But it is not used in this work because it is just too outdated. The treatment of non-linear effects at high energies and small impact parameters is not included and the last time it was tuned to accelerator data the LHC was still under construction. Figure 4.7 gives an impression of how much the model variates from more recent lepton flux calculations.

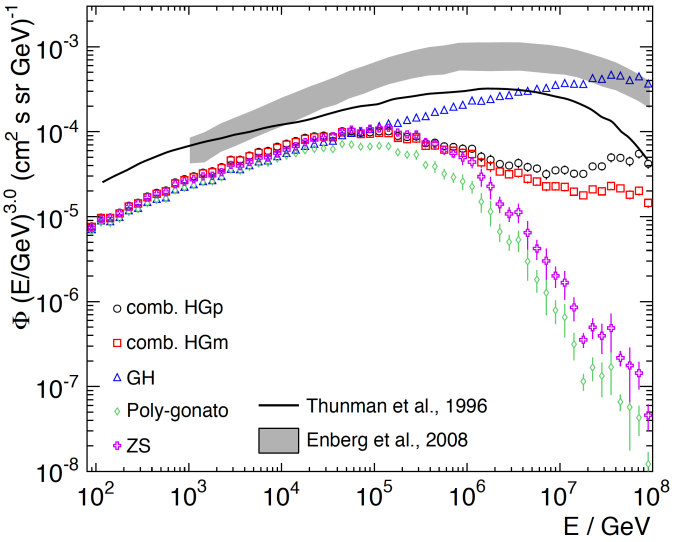

Figure 4.7: Flux of leptons originating from charm particles with the QGSJET 01C model. Figure adopted from [FTD12].

EPOS-LHC is the by far most complex model of those described here and the calculation time with CORSIKA is considerably longer when using it. As the name suggests, the model was developed with a primary focus on accelerator experiments. It also uses the Gribov-Regge theory but not the classical approach like SIBYLL and QGSJET but a parton based one which ensures energy conservation at amplitude level. For our purpose here this model has the disadvantage that not that much effort has been put into the extrapolation to ultra-high energies, e.g., just like for QGSJET 01C, non-linear effects at high energies and small impact parameters are not accounted for properly. But what ultimately rules it out for most analyses in the following is that it, too, does not support

the production of charmed hadrons. It will be used for the error analyses.

DPMJET-III is the last model to be discussed here. Like SIBYLL it is a **D**ual **P**arton **M**odel and is similar in other regards as well. But there is a known problem with an unphysical, technical limitation at high energies above some PeV. Though there is a recently revised version, DPMJET-III 20171, which fixed many problems, we still cannot use the model in the high energy regime. Figure 4.8 shows a comparison of the different models and one can clearly see that the muon flux predicted by employing DPMJET-III skyrockets at around 10^7 GeV and is not at all comparable to the predictions of the other models anymore. For this reason, the model will not be used for any high energy calculations here. In the low energy region, however, it does play a role because MCEq employs it as low energy extension for the other interaction models for energies below 80 GeV.

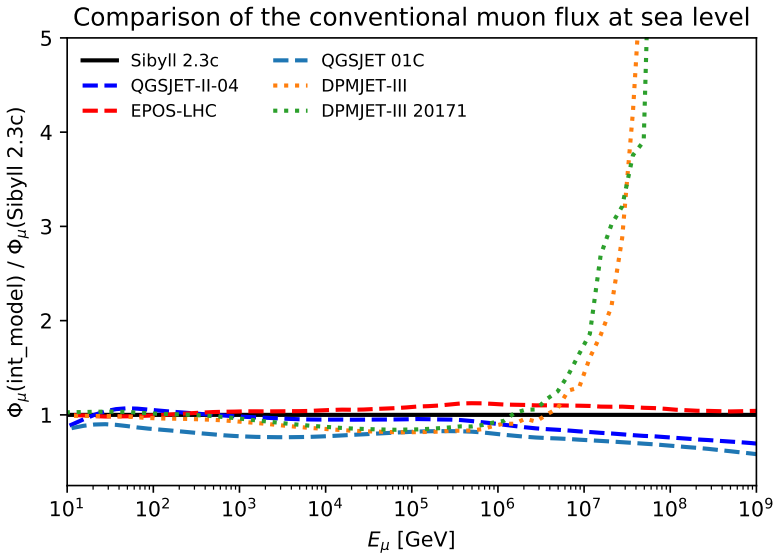

Figure 4.8: Comparison of the predicted muon flux calculated by the different interaction models for a zenith angle of 0° at sea level. Calculation were done with MCEq, employing the US-Std atmosphere and TIG as primary model.

4.4 CORSIKA and further processing

CORSIKA [Hec+98], which stands for **Co**smic **R**ay **Si**mulations for **Ka**skade, is the most commonly used Monte Carlo program to simulate cosmic ray air showers in detail [Hec01]. Simulations are run separately for different primary particles whose initial energy is random, following a predefined distribution. The shower initiated by such a primary particle is then simulated in detail as a stochastic process and the particles are tracked on their way until they interact with nuclei in the air or decay or they reach ground.

The particle content of the atmosphere and the hadronic interactions are described by the respective models discussed above.

The distribution from which the primaries are drawn randomly is usually not one of the sophisticated primary flux models discussed above but a rather simple one. For the KM3NeT production it is an E^{-1} spectrum with a minimum energy of 1 TeV and a maximum energy of 1 EeV. That means that after the production the events need to be re-weighted according to a realistic primary flux model.

That CORSIKA simulates air showers in such detail leads to an major drawback: calculations are very time consuming. To get a production large enough to work with would take hundreds of years on one modern CPU, thus Computer clusters have to be used and even then the calculations might take several month. When working with a CORSIKA production that is not too large one might run into problems because the weighting process described above can lead to large statistical errors.

When a production is large enough is difficult to determine beforehand and often a smaller production is calculated and analysed before the month long calculation gets started. In the KM3NeT collaboration exactly this was done and an initial 1% production was simulated. It consists of shower data from a million primaries, drawn from the distribution described above. It is estimated that a total of 10^8 starting events will be needed, thus the name of this initial production. SIBYLL 2.3 and the KM3NeT-Std atmosphere were used as interaction and atmospheric model respectively.

CORSIKA, being written only for the simulation of air showers, is not able to propagate particles down through sea water to the detector; other software is needed for this. Only muons and neutrinos will be propagated further and we focus here on the former. The largest fraction of other particles will not make it down to the detector because interactions are too likely in water or the energy loss is too large. The CORSIKA output is first transformed to a different data format for which the software CORANT (**cor**sika to **ant**ares) was written and used already for KM3NeT's predecessor ANTARES [Age+11]. Then these data are feeded to another software called PROPA which employs MUSIC [Ant+97] to propagate muons from sea level to the detector. MUSIC was originally written for the propagation in rock but when changing some parameters it can also be used for sea water. it treats all processes of muon interaction with matter with high energy loss as stochastic processes – a level of details we do not have in our alternative approach presented in the next section.
A much more detailed description of the simulation chain discussed here can be found in [Hei17] and more information about the KM3NeT CORSIKA production is available in the internal Wiki* for members of the collaboration.

When investigating the thus far produced muon events at detector level it turns out that they are by far too few for an analysis of the prompt flux, the main subject of this thesis. There is a total of 13 354 193 muons (2 736 428 from protons as primaries, 1 539 522 from He, 2 211 605 from Mg, 2 088 292 from Ni, 2 123 754 from O and 2 654 592 from Fe nuclei) reaching the *can*, a volume defined as the instrumented volume of one ARCA building block plus three times the absorption lengths of light in water in all

*`https://wiki.km3net.de/mediawiki/index.php/Simulations/CORSIKA`

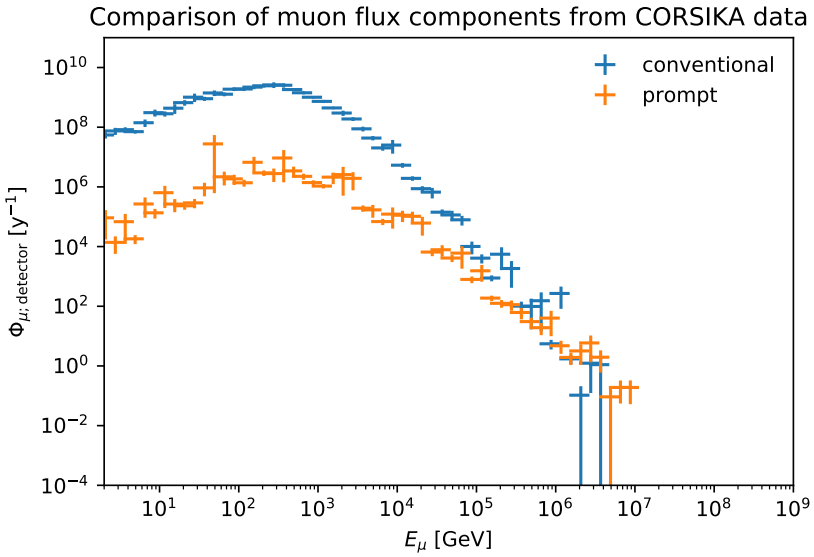

Figure 4.9: Muon energy histogram of the initial 1% CORSIKA production, resolved for the conventional and prompt component.

directions. The events are then weighted, depending on their primary's energy, to the GST 3-gen primary flux model that we discussed in section 4.1. Figure 4.9 shows an energy histogram of all the events together, resolved for the conventional and prompt component. As one can see, acceptable error bars can be found for the low energy conventional flux but not for the prompt flux, especially not in the high energy region of around and above 10^6 GeV which will turn out to be the most interesting region. For this reason we will not use CORSIKA for any analyses in the following and will instead rely on MCEQ. But there is a reason for having it introduced: MCEQ was not written to calculate fluxes below sea level and was thus extended by the author. A comparison with the CORSIKA production helped in finding errors and, after eliminating many, serves now as a "proof of concept".

4.5 The Matrix Cascade Equation Solver (MCEq)

As discussed in the last paragraph, calculations with CORSIKA tend to be time consuming, sometimes too time consuming, and this was the motivation for A. Fedynitch et. al. to develop another approach, e.g. to make comparisons of different models easier [FTD12]. That turned out to be MCEQ [Fed+15] which is a very efficient method for the calculation of atmospheric lepton fluxes with no statistical error (except Poisson). These calculations usually take less than a minute for a given zenith angle on an average laptop bought in 2015. Some for our purposes necessary extension to the program as well as the necessity to calculate fluxes over the whole range of zenith angles, from vertically

to horizontally entering particles, extend the calculation time to several minutes, in some cases hours, but it is still incredibly fast compared to CORSIKA.

This efficiency comes, of course, with a price and there are reasons for CORSIKA still being an indispensable tool for cosmic ray experiments: MCEQ only calculates fluxes but does not produce separate shower events which can then be used for further processing. The CORSIKA production and the further propagation with PROPA are only the first links in a larger simulation chain which is common for experiments like KM3NeT. For particles reaching the detector other programs simulate the production of Cherenkov light, the response of the PMTs and so forth. This is an important part of understanding the detector in order to learn how to analyse real data. For that task, MCEQ cannot replace CORSIKA. And also things like bundle multiplicity cannot be investigated. But since we are only interested in the muon flux here, MCEQ it does just fine.

A short explanation of how MCEQ works can be found in [Fed+15] and a brief overview heavily based on that publication will be given here. The main paper is yet to be published, the code is made publicly available on GitHub*.

4.5.1 The basic concept

The approach is based on numerically solving the cascade equation which was discussed in section 2.3 for all the different particles playing a role in air showers. In order to be able to make use of modern implementations of linear algebra algorithms the coupled cascade equations are rewritten into a matrix form in the implementation. The fluxes are calculated for discrete energies which are logarithmically spaced between 50 GeV and 10^{10} GeV with roughly eight bins per decade of energy. The fluxes $\Phi_h(E_i)$ for the different particles h and energies E_i are then grouped together into a column vector

$$\mathbf{\Phi} = \begin{pmatrix} \Phi_p(E_0) \\ \Phi_p(E_1) \\ \cdots \\ \Phi_p(E_N) \\ \Phi_n(E_0) \\ \cdots \end{pmatrix} \tag{4.5}$$

whose dimension is then of the order of ~ 6000.

Then reciprocal coefficients $1/\lambda$ for the interaction and decay length, $\mathbf{\Lambda_{int}}$ and $\mathbf{\Lambda_{dec}}$ are listed in diagonal matrices, i.e. for the interaction lengths

$$\mathbf{\Lambda_{int}} = \mathrm{diag}\left(\frac{1}{\lambda^p_{int,E_0}}, \ldots, \frac{1}{\lambda^p_{int,E_N}}, \frac{1}{\lambda^n_{int,E_0}}, \ldots, \frac{1}{\lambda^n_{int,E_N}}, \frac{1}{\lambda^{\pi^+}_{int,E_0}}, \ldots \right). \tag{4.6}$$

The decay lengths matrix is constructed similarly but there the air density is factored out.

*`https://github.com/afedynitch/MCEq`

Then a matrix for the interactions $\mathbf{C}$ and one for the decays $\mathbf{D}$ is constructed like

$$\mathbf{C} = \begin{pmatrix} \mathbf{C}_{p\to p} & \mathbf{C}_{n\to p} & \mathbf{C}_{\pi^+\to p} & \dots \\ \mathbf{C}_{p\to n} & \mathbf{C}_{n\to n} & \mathbf{C}_{\pi^+\to n} & \dots \\ \mathbf{C}_{p\to \pi^+} & C_{n\to \pi^+} & \mathbf{C}_{\pi^+\to \pi^+} & \dots \\ \vdots & \vdots & \vdots & \ddots \end{pmatrix} \tag{4.7}$$

where the sub-matrices are defined as

$$\mathbf{C}_{l\to h} = \begin{pmatrix} c_{l(E_0)\to h(E_0)} & \cdots & c_{l(E_0)\to h(E_N)} \\ & & c_{l(E_1)\to h(E_0)} \\ & \ddots & \vdots \\ 0 & & c_{l(E_N)\to h(E_N)} \end{pmatrix}. \tag{4.8}$$

Taking everything together on can write the coupled cascade equation in its matrix form as

$$\frac{\mathrm{d}}{\mathrm{d}X}\mathbf{\Phi} = \left[(-\mathbf{1} + \mathbf{C})\mathbf{\Lambda_{int}} + \frac{1}{\rho(X)}(-\mathbf{1} + \mathbf{D})\mathbf{\Lambda_{dec}}\right]\mathbf{\Phi}. \tag{4.9}$$

This equation can then be numerically integrated very efficiently, starting at the top of the atmosphere and then going down with an adaptive step size until reaching ground level. Usually some approximations are being made; for the details on this we refer to the paper [Fed+15].

All the different primary flux models discussed in section 4.1 and more can be used as boundary condition and the different atmospheric models discussed in 4.2 can be used directly and enter in the calculation of the gain in slant depth which is an integration over the density for the individual steps. Also all the different interaction models that were topic in 4.3 can be employed. They determine the values in the interaction matrix $\mathbf{C}$. The models are incorporated in form of tabulated data for cross sections and particle yields for the discrete energy bins and, since the values have already been calculated and stored, the calculation time for the different models does not vary much.

4.5.2 The extension for KM3NeT

Just like CORSIKA, MCEq was developed for the analysis of extensive air showers. The propagation of particles from sea level downwards and functions to calculate the flux according to a certain detector geometry are not part of the program. Admittedly, there is a class that allows to define layers of general targets but it is either that or an atmospheric model. Furthermore parameters for the energy loss in media other than air are not integrated. For this reason MCEq had to be extended.

In writing the extension it was tried to change as few things as possible from the original program. The flux calculations at sea level are performed as usual and then the flux vector $\mathbf{\Phi}$ is copied and all fluxes expect the one for muons are set to zero*. Thus,

*A technical reason for this is that a calculation with the complete flux vector lead to errors which are

just like for CORSIKA, only muons are propagated to the detector. Then the calculation is continued in water just like it was in the atmosphere but now with a fixed density of 1.025 g/cm^2 and different values for the energy loss that were derived from PDG data and an extrapolation thereof as was discussed in section 2.5. In a first step the flux at the top of the detector is calculated and then one can go deeper in steps of ones choosing. MCEQ provides geometric formulae with which the earth curvature can be taken into account when the distance from sea level to the detector is calculated for different zenith angles. But even then the distances become quite large for large angles and since the step size has to be kept relatively small, i.e. a few meters, because of the much larger density and thus much faster gain in column depth in water the calculations might take a couple of minutes.

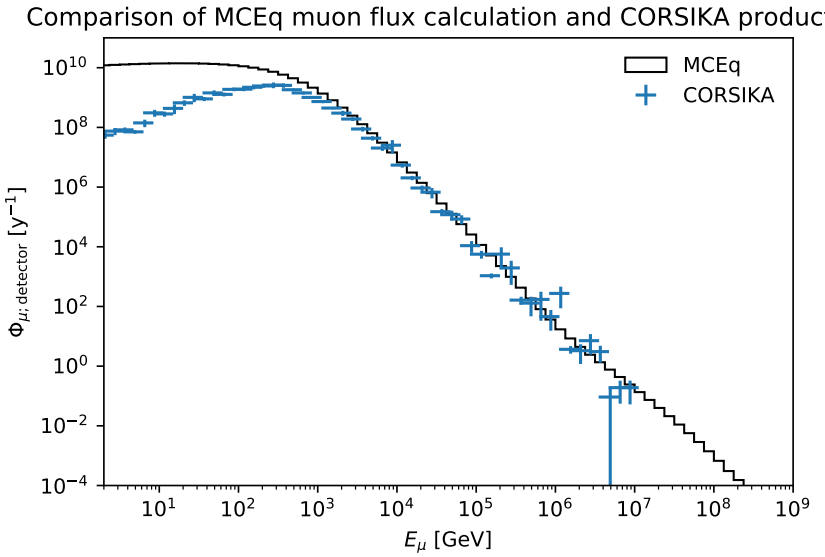

Figure 4.10: Comparison of the total muon flux calculated with MCEQ and CORSIKA respectively without a change of MCEQ's energy loss function. The GST 3-gen primary model with a cut-off below 1 TeV and above 1 EeV, the KM3NeT-Std atmosphere, and SIBYLL 2.3 were employed in both cases. Plotted is the yearly flux at the can, the instrumented volume of one building block extended by three absorption length of light in water.

Having implemented all the extensions the flux calculations were tested against the data from the CORSIKA production. How that worked out is shown in Figure 4.10. As one can see the agreement is quite good for high energies above 10^4 GeV but for low energies the calculated fluxes differ up to a factor of more than 100. The reason for this turned out to be the original energy loss function which was written for air and cannot handle the larger losses in the by far denser sea water. To understand this better we will

not yet fully understood.

now take a look on how the energy loss is originally implemented in MCEq and then on how this was fixed.

Since MCEq only operated with fluxes, the energy loss works directly on the level of histograms. When the energy loss after travelling through a certain slant depth is calculated, the boundaries of the energy bins are shifted by a tabulated value for the energy loss times the change in slant depth. Afterwards the new centres and bin widths are calculated. Then a linear interpolation between the shifted bin values (the shifted value equals the new centre times the new width) is performed in log space. From this interpolated function, the values at the centres of the old bins are calculated and then divided by the old bin widths, giving the updated flux for the original energy grid*. If one takes a moment to think about this implementation of the muon energy loss, one will realise that such a drop at low energies that we see in Figure 4.10 can simply not happen when the spectrum at sea level falls monotonously with the energy as it usually does. Thus it became necessary to completely rewrite the energy loss function.

The basic idea of calculating the energy loss at the level of histograms remains the same. Again, the shift of the bin boundaries is calculated according to the same tabulated energy loss data used above. But this time no interpolation is performed. Instead it is calculated how much of the area of a bin is shifted below the original upper boundary of the bin next to it on the left – in logarithmic space. Then this overlap is subtracted from the bin and added to the bin on the left next to it (if there is one). It is taken care that the gain in slant depth is never that high such that parts of one bin get shifted further than to the one right next to it. This procedure may sound overly simple but is very efficient and actually seems to work. Figure 4.11 shows a comparison between the old and new energy loss functions. The difference in the low energy region is quite large – just as was needed – whereas at energies from slightly above 10 TeV the difference between both fluxes is less than 1%.

How well MCEq with the updated energy loss agrees with what was calculated by Corsika and Music can be seen in Figure 4.12. It is quite remarkable how one can get to such a good agreement with such primitive methods, also keeping in mind that thinks like e.g. critical energy losses are not at all accounted for MCEq. There certainly are still some differences but the histograms undeniably are very similar still which is why we think we can indeed rely on the extended MCEq for this preliminary analysis.

*The details of this calculation depend on the kernel that is used by MCEq. The process described here will be performed if one uses the MKL kernel, based on Intel's Math Kernel Library, which one should if possible because it is the fastest.

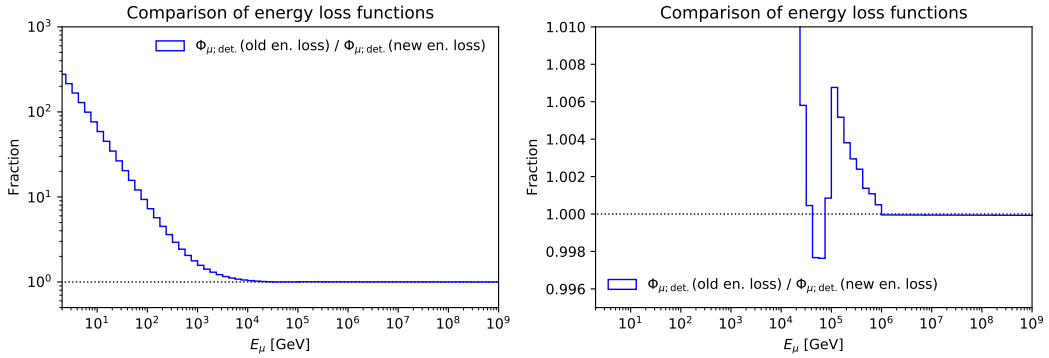

Figure 4.11: Comparison of the total muon flux calculated with MCEq's original and updated energy loss function. The GST 4-gen primary model, the KM3NeT-Std atmosphere, and Sibyll 2.3c were employed in both cases. Plotted is the yearly flux at the can, the instrumented volume of one building block extended by three absorption length of light in water.

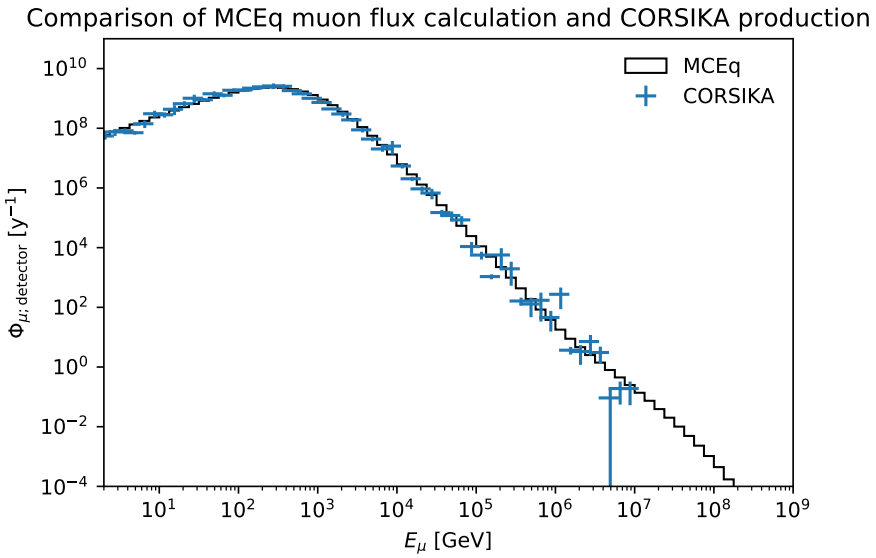

Figure 4.12: Comparison of the total muon flux calculated with MCEq and Corsika respectively with the update of MCEq's energy loss function. The GST 3-gen primary model with a cut-off below 1 TeV and above 1 EeV, the KM3NeT-Std atmosphere, and Sibyll 2.3 were employed in both cases. Plotted is the yearly flux at the can, the instrumented volume of one building block extended by three absorption length of light in water.

Chapter 5

Results

In this chapter the results of this thesis are being presented. We will first take a look at the energy distribution of the muon flux, resolved for the conventional and prompt flux components. Then the influence of a different atmospheric model which is used for some other calculations will be investigated, followed by a comparison of different primary flux and interaction models, the latter for conventional flux only.

The second section will be about the angular distribution. Again we will look for regions were the prompt flux might be measurable but will find no promising results here. Especially at large angles the muon flux produced by neutrinos would be needed to be taken into account in order to make any deductions.

Then there will be a section about seasonal variations of the muon flux and we will compare flux data from January and July over the full spectrum of energy and zenith angle. On the one hand this is interesting because it was suggested one might get information about the prompt flux as well as the pion to kaon ratio from the measurements of such variations but they are also interesting in their own right.

At the end an attempt is made to calculate how well, with which significance after which time, KM3NeT/ARCA might be able to measure the prompt muon flux. For this error estimates from the first section of this chapter are being used, but also errors in the measurement and reconstruction process are taken into account. The result presented in the end will be made under the very strong, at this moment admittedly unrealistic, assumption that all the muons arriving together in a bundle can be resolved.

5.1 Energy distribution

Figure 5.1 shows one of the main results of this thesis. It is an energy histogram of the muon flux at the KM3NeT/ARCA detector which was calculated using our reference models GST 4-gen and Sibyll 2.3c for the primary flux and interactions respectively. For this one case the NRLMSISE-00 atmospheric model was employed in full detail, meaning an atmospheric density profile has been calculated separately for each day of

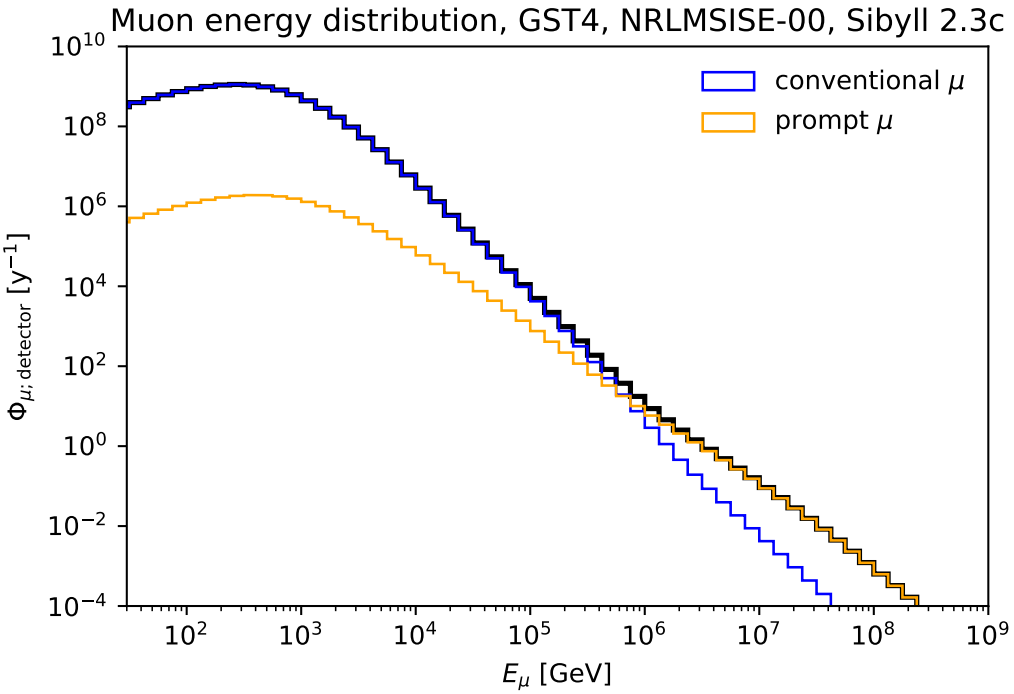

Figure 5.1: The energy distribution of the muon flux at the KM3NeT/ARCA detector, resolved for the conventional and prompt component. The GST 4-gen model was used to model the primary flux and Sibyll 2.3c for the interactions. As for the atmosphere, the NRLMSISE-00 model was used and the flux was calculated separately for each day of the year and then added together.

the year and then been used to calculate the muon flux.

At low energies up to some 10^5 GeV the muon spectrum is, unsurprisingly, completely dominated by the conventional flux. But around 10^6 GeV where most pions and kaons undergo re-interaction rather than decays, the prompt flux starts to dominate the spectrum. For this reason the spectrum becomes harder in the high energy region, modelling approximately the primary spectrum, whereas for low energies the muon spectrum is about one power of the energy steeper than that of the primaries.

At energies where the prompt flux is relevant, the total count is already relatively low. But we will find later that despite this a measurement of the prompt component could be possible after a few years. Unfortunately, in this high energy region the uncertainties of the primary flux and interaction models become large. To get an estimate on this comparisons with the different models are done. Before that a brief comparison of atmospheric models needs to be made.

5.1.1 Comparison of atmospheric models

The calculation of the energy histogram in Figure 5.1 took quite some time, at least by the standards of MCEq, because 365 calculations for the different days of the year had to be performed*. Thus for the calculations that are used to investigate the influence of different primary flux and interactions models the KM3NeT-Std atmosphere was used instead of employing the NRLMSISE-00 model.

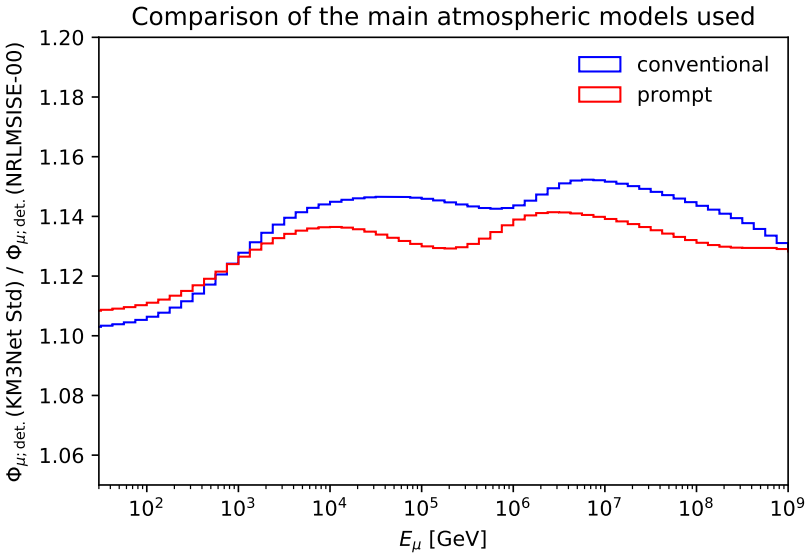

Figure 5.2: Comparison of the energy distributions of the muon flux at the KM3NeT/ARCA detector for two different atmospheric models. Shown is the flux calculated with the KM3NeT-Std atmosphere compared the the flux calculation when using the full NRLMSISE-00 model for each day ot the year resolved for the conventional and prompt component. The GST 4-gen model was used to model the primary flux and Sibyll 2.3c for the interactions.

Figure 5.2 shows a comparison of the flux predictions of the different atmospheric models. With the KM3NeT-Std atmosphere the calculated muon flux turns out to be 10% to 15% higher then when using the more complex model. Apart from the different modelling of the atmosphere one reason for this might also be that KM3NeT-Std atmosphere was derived for the Corsika production of the whole KM3NeT experiment and not specifically for the position of ARCA.

The variation of the conventional and prompt flux at least behave similarly and since for the following comparisons only fractions are relevant it was decided that the primitive atmospheric model can be used despite the differences to the sophisticated one.

*The final result was multiplied by 365.25/365 in order to account for leap years. Data for 29th February are not included in the model used.

5.1.2 Comparison of primary flux models

In section 4.1 different models of the cosmic ray primary flux were explained in some detail. The GST 4-gen model turned out to be the most sophisticated one, matching the data best, and was thus chosen as the reference model. But as was also discussed there the errors on data in the high energy region are very large because measurements can only be performed indirectly by analysing data of extensive air showers. In order to get an error estimate the muon flux calculations for the different primary models are being compared here.

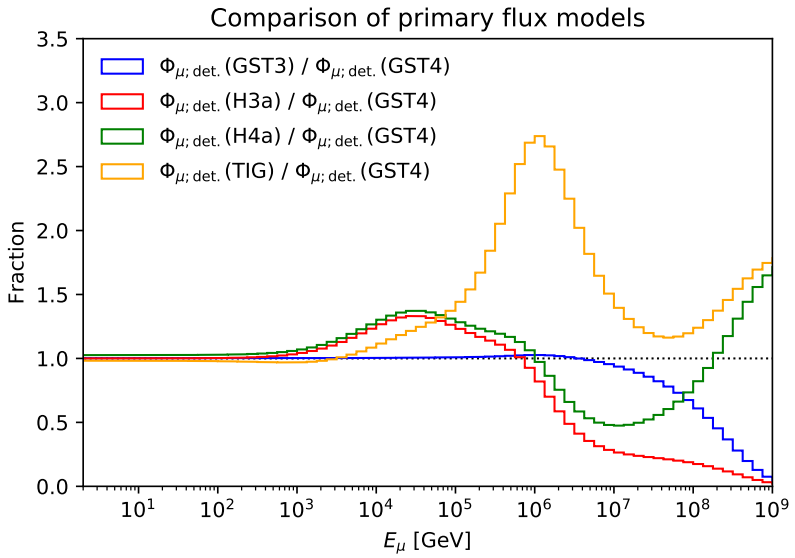

Figure 5.3: Comparison of the energy distributions of the total muon flux at the KM3NeT/ARCA detector for the different primary flux models discussed in section 4.1. Shown is the flux calculated with different models compared the the flux calculation when using the reference model GST 4-gen. The KM3NeT-Std atmosphere was used and Sibyll 2.3c for the interactions. The same comparison was also done for the conventional and prompt flux separately but the result was qualitatively the same.

The first thing to notice when looking at Figure 5.3 is that the fluxes agree very well for energies up to 1 TeV but very large deviations can be found in the high energy region. Another interesting thing is that the composition of the flux does matter indeed. In Figure 4.3 one can see that the particle flux of the TIG model is the lowest over almost the entire energy spectrum range but it leads to the largest muon flux still. Thus we find confirmed again here that not the number of nuclei per energy but rather the number of nucleons per energy-per-nucleon is the more relevant parameter for atmospheric lepton fluxes. This also explains the large difference between the H3a and H4a model for the latter of which the last generation consists of proton only.

5.1.3 Comparison of interaction models

Although it was found in section 4.3 that SIBYLL is the only interaction model we can use for an analysis of the prompt flux it is far from being perfect and uncertainties in the high energy regions are large. An error estimate on the total flux due to the interaction model cannot be derived here but when doing the significance analysis in section 5.4 an error estimate on the conventional flux is needed and that we can actually do. Besides SIBYLL we have to other state of the art interaction models, QGSJET-II-04 and EPOS-LHC, that are perfectly capable of performing conventional flux calculations.

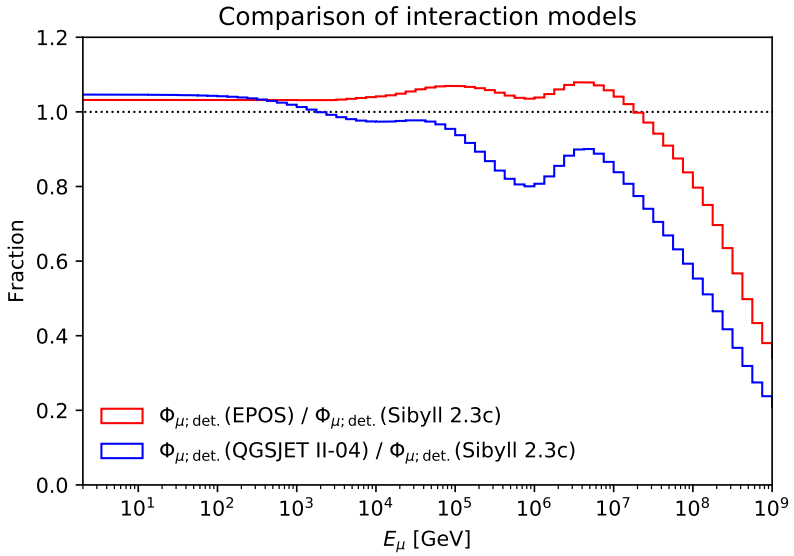

Figure 5.4: Comparison of the energy distributions of the conventional muon flux at the KM3NeT/ARCA detector for different interaction models discussed in section 4.3. Shown is the flux calculated with different models compared the the flux calculation when using the reference model SIBYLL 2.3c. The KM3NeT-Std atmosphere was used and and GST 4-gen as the primary model.

What can be found from Figure 5.4 is that the models agree considerably well up to a little above LHC energies but then deviate a lot, especially in the ultra-high energy region. Whereas in the low energy region SIBYLL 2.3c produces the fewest muons of the models considered, it is placed well between the other two models in the region of 10^3 GeV to $2 \cdot 10^7$ GeV (just as could be expected from Figure 4.8) up from where it then produces a much larger muon flux than QGSJET-II-04 and EPOS-LHC.

5.2 Angular distribution

Having found a clear signal of the prompt component in the energy regime, now the zenith angle distribution of the atmospheric muon flux is discussed. Fluxes were calculated for 50 different angles, equally spaced in $\cos\theta$ between 0 and 1. MCEq does not allow for the calculation of fluxes for a zenith angle larger than 90°, i.e. $\cos\theta < 0$. It would in principle not be too difficult to extend the program to go a few degrees below the horizon (as long air and water remain the only media travelled through) by performing calculations a few degrees off on the earth's angular grid but as we see in this section that is not at all necessary because the to be expected fluxes would by completely negligible.

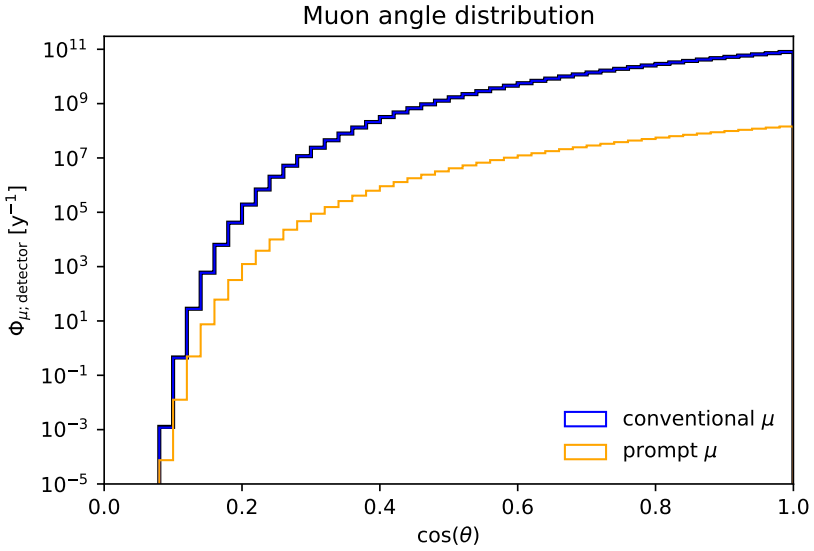

Figure 5.5: The zenith angle distribution of the muon flux at the KM3NeT/ARCA detector, resolved for the conventional and prompt component. The GST 4-gen model was used to model the primary flux and Sibyll 2.3c for the interactions and an energy threshold was set at 30 GeV. As for the atmosphere, the NRLMSISE-00 model was used and the flux was calculated separately for each day of the year and then added together.

Figure 5.5 shows a plot of the angular distribution, resolved for the conventional and prompt component as it was done for the energy in the previous section. The overall shape of the total flux as well as that of the separate components looks in logarithmic space like a shifted logarithmic function. Coming from the right at large $\cos\theta$, i.e. vertically entering particles, the flux at first falls slowly when going to the left, i.e. lager zenith angles, and then more and more rapidly. At around $\cos\theta = 0.1$, i.e. $\theta = 84°$ the predicted flux has become so small that not a single event can be expected at a running time of the detector of even a few decades.

One question asked in this thesis is whether the to be expected angular distribution

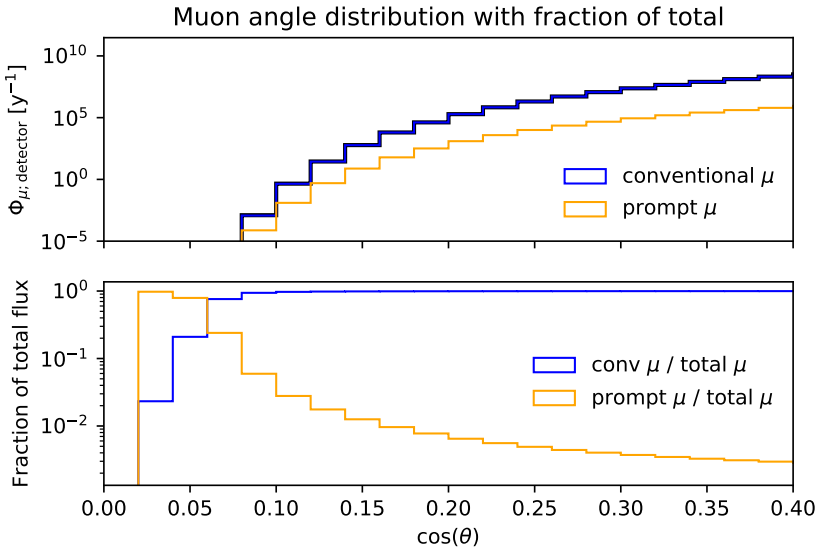

Figure 5.6: The zenith angle distribution of the muon flux at the KM3NeT/ARCA detector, based on the same data as in Figure 5.5, zoomed in to the region of zenith angles larger than $\theta = 66°$ down to the horizon. On the top the total flux is shown again whereas the histogram on the bottom shows which flux component dominates at a certain angle.

might also have a measurable signature of the prompt muon flux component. The answer to this, unfortunately, is a definite no. Figure 5.6 shows very clearly why this is: In the region where the prompt flux makes up for enough of the total flux to be measurable, less than one muon in 10 000 years is to be expected. Analyses were run with different energy thresholds but did not lead to anything useful.
Additionally, at zenith angles above $\cos\theta = 0.25$ or $\theta \backsimeq 75°$, an additional component to the muon flux needs to be taken into account, as can be seen from Figure 5.6. Muons produced by atmospheric neutrinos which are interacting with nuclei in the sea. For large zenith angles these neutrino induced muons will dominate the spectrum and there is no promising method to disentangle the two contributions.

5.3 Seasonal variations

In section 2.4 we established that the muon flux variates with season. In this section we will discuss which variations are to be expected for KM3NeT/ARCA and explain their energy and zenith angle dependence*. One reason why seasonal variations are interesting

*A note for the corrector: Large parts of this section have already been presented in one of the author's research project report. There the focus was on KM3NeT/ORCA but the explanations are all the same.

is that they might help to measure the prompt flux [DG10] and determine the pion/kaon ratio [Des11].

The reason for the seasonal variations is the following: As was already discussed in section 2.4, when particles like pions and kaons are produced by cosmic ray interactions in the atmosphere, there is a competition whether they are going to decay, leading to muons, or interact again. This depends on the local density of the atmosphere: a less dense (hotter) atmosphere benefits decay whereas a denser (colder) atmosphere leads to a higher probability for interaction [Roc09].

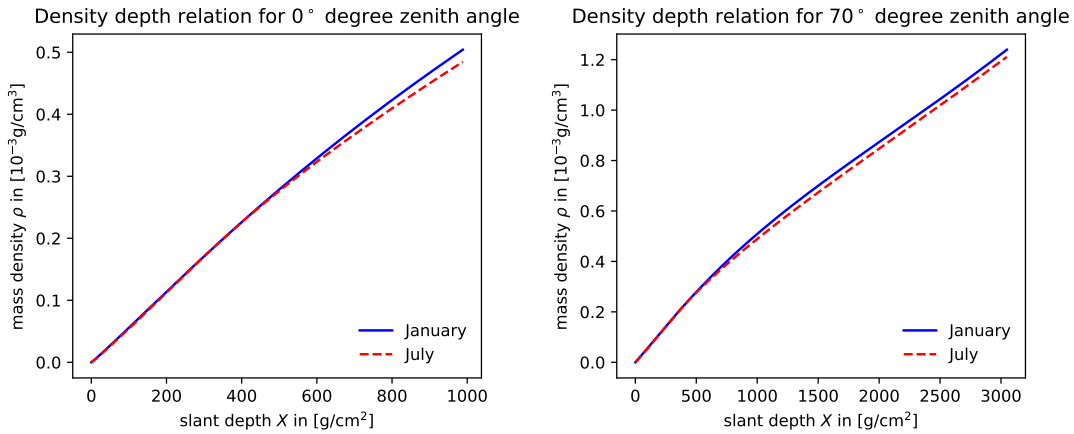

Figure 5.7: Relationship between atmospheric depth and density for a zenith angle of 0° (left) and 70° (right). Note the different scaling of the x-axis.

Figure 2.3 shows the flux of different particles in the atmosphere depending on the atmospheric depth. One can sea that the pions, the main contributor to the muon flux at lower energies, have their maximum at an atmospheric depth of around 150 g/cm^2 and then the number falls approximately exponentially as the pions either interact or decay to muons and the corresponding neutrinos. As can now be seen from Figure 5.7, the atmosphere in winter is always at least as dense and for the some part denser than in summer for a depth above 150 g/cm^2 which makes it more likely for particles like pions to interact instead of decay what then lowers the expected muon flux compared to summer.

In Figure 5.8 the main result of this section is shown. What is depicted there is a colour-coded map of the fraction of the expected muon flux at the ARCA detector in summer divided by the expected flux in winter over the entire energy range anf for all the relevant zenith angles up to $\theta = 75°$. The total variation, integrated over angle and energy, is only 1.67%. This is, however visible, well below what has been measured with IceCube [Gai], around 10%, but this is not surprising since a larger variation is expected at the poles [Hon+15b].

Why Figure 5.8 looks as it does es best explained when looking at the seasonal flux variations at sea level because the explanation involves critical energies which are not

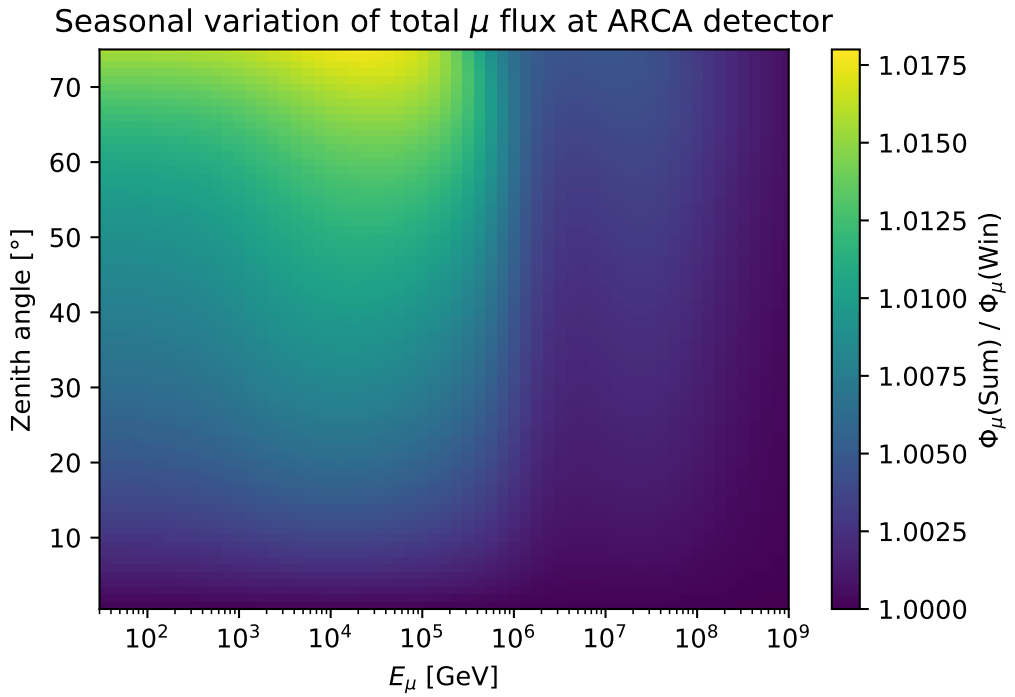

Figure 5.8: Seasonal variation of the KM3NeT flux at the ARCA detector. What is here shown colour-coded is the expected muon flux in summer divided by the expected muon flux in winter for zenith angles between 0° an 75° degrees. For the flux in summer the NRLSMSISE-00 atmospherec profile for 1st July was employed, 1st January represents the winter. As usual, GST 4-gen describes the primary flux and Sibyll 2.3c the interactions.

well defined at detector level and also features are more distinct.

Figure 5.9 shows the flux varition at sea level of which Figure 5.8 is just a smeared out version where all features are shifted to the left, the more the larger the zenith angle. One can note at least five important features in this figure:

1. The flux in summer is indeed larger than the flux in winter.
2. The difference grows towards larger zenith angles.
3. There is hardly any difference at the lowest energies.
4. There is hardly any difference at high energies.
5. For very large zenith angles and low energy, we find a larger muon flux in winter than in summer.

The first point has already been explained above: Below the production height of parent particles the atmosphere is less dense in summer (see figures 2.3 and 5.7) and so these

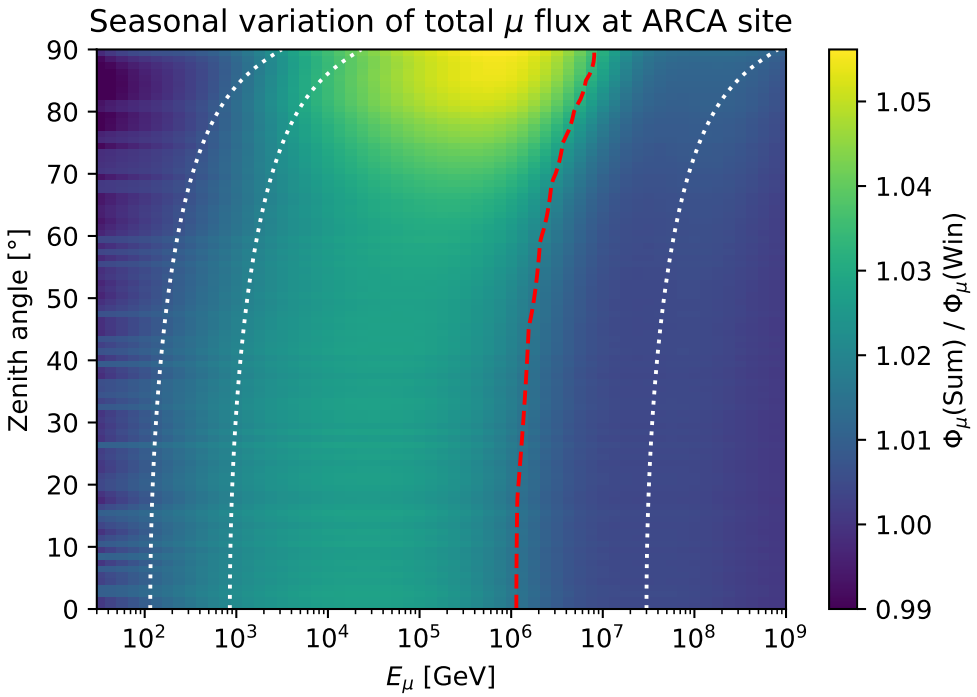

Figure 5.9: Seasonal variation of the KM3NeT flux at the ARCA site at sea level. What is here shown colour-coded is the expected muon flux in summer divided by the expected muon flux in winter for zenith angles between 0° an 90° degrees. The white dotted lines indicate the critical energy for $\pi^{\pm}$, $K^{\pm}$, and $D^{\pm}$ (from left to right). The red line indicates where the prompt flux starts to dominate the spectrum. The employed models are the same as in Figure 5.8.

are less likely to interact again than to decay which leads to a higher muon production rate.

The second point, the growing difference with larger zenith angle θ, can also be explained by figures 2.3 and 5.7. For larger angles, the parent particles are produced higher (compared to vertically travelling particles) in a less dense medium in which they travel for longer, such that differences in the local density can make a larger difference on the muon production rate.

To explain the third point, we invoke the critical energy E_{crit} defined in Equation 2.10 which is the energy below which interaction and above which decay is more probable. Table 2.1 gives the values of ϵ_P for vertically entering particles for the relevant atmospheres. The values of the KM3NeT-Std atmosphere values used for the dotted lines in Figure 5.8 and 5.9.

The two upper rows of plots in Figure 5.10 come in to explain why there is hardly any difference at the lowest energies. From the top right plot one can clearly see that muons

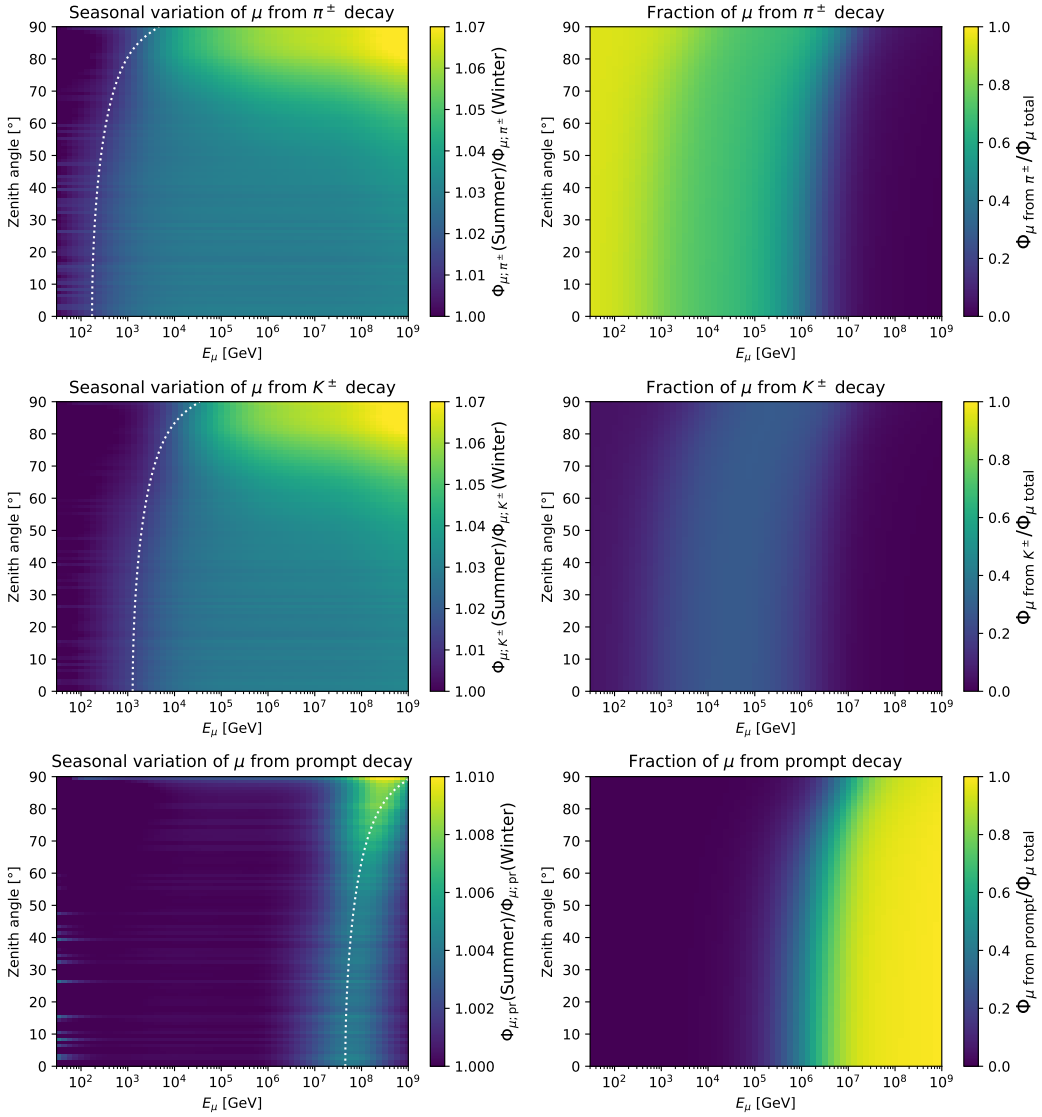

Figure 5.10: A more detailed look at the different contributions to the muon flux. The plots on the left show how the muon flux changes seasonally for different contributors, resolved for $\pi^\pm$, $K^\pm$, and prompt particles. The dotted white line indicates the critical energy. On the right side the contribution the respective parent particles to the total muon flux is shown.

originating from pion decay dominate the flux at low energies and kaons start to play a role at around 10^3 GeV (middle right). On the left, the seasonal variation for the muon

flux originating from the decay of the respective particles is shown separately and what one can see here is that the variations start to become visible only around the critical energy ϵ_P since well below this energy decay is very likely in both cases, leaving not much space for a variation with the seasons.

The red line in Figure 5.9 and the last plot of figure Figure 5.10 explain the fourth point on the list, namely why there is hardly any difference at high energies. In the indicated region the prompt flux starts to dominate the spectrum, i.e. muons from particles with very short lifetimes ($\lesssim 10^{-12}$s) which almost certainly decay anyway, giving not much room for variations with density of the surrounding medium and thus season. The lightest of these particles are $D^{\pm}$ mesons and the effect of their critical energy can be seen in the second last plot of Figure 5.10. It is not as clear as for pions and kaons and one explanation for this is that the prompt flux consist of more than just $D^{\pm}$ as was discussed in section 2.4. To resolve for all the different contributions to the prompt flux would just result in another bunch of coloured plots and is not seen as instructive here.

The last point, the larger muon flux in winter than in summer for low energies and high zenith angles, is caused by muon decay. Figure 5.11 compares the seasonal flux variation discussed above with a different calculation thereof where the muon decay has been deactivated.

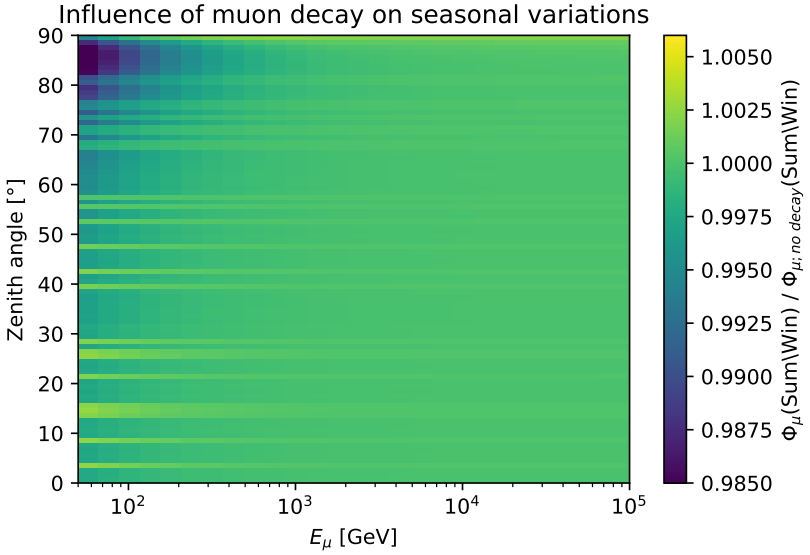

Figure 5.11: Influence of the muon decay on seasonal variations. Here plotted is the seasonal flux variation divided by a different calculation thereof where the muon decay has been deactivated.

From this one can see clearly that the drop in the muon flux in summer compared to winter at low energies and high zenith angles is indeed caused by muon decay. As the physical reason for this the author assumes the following:
For a large part the atmosphere is denser in summer than in winter (cf. Figure 4.5)

which should have the effect that for large zenith angles some fraction of the muons is produced higher in the atmosphere in summer than in winter. Since the zenith angles are large, these muons have quite some distance to travel, more in summer than in winter, and when there energy is sufficiently low, a good fraction of them might decay, more for a larger distance, i.e. in summer.

The occasional "horizontal stripes" in Figure 5.11 are not assumed to be of physical origin but rather are numerical artefacts. The author guesses this has to do with the different distances through the atmosphere for different zenith angles and the stepsize adaptation when numerically integrating over the slant depth.

5.4 Estimating a significance

One of the main goals of this work was to find our whether or not the prompt component of the muon flux might be measurable for KM3NeT/ARCA. As discussed in the previous sections, the prompt component is clearly visible in the energy histogram but not when one resolves for the zenith angle. The mentioned idea to get information about the prompt flux from seasonal variations could not even be employed for the much larger fluctuations of IceCube [DG10] and it will not be used here either. Thus only the energy distribution will be taken into account in the following.

What will actually be compared here is the following: The total flux is what one day will be measured and in this analysis we treat it as such which means that the error put on it will be errors of the detector, not the simulation. The flux it will be compared to is the conventional flux which even when the experiment is running will be a simulated quantity and comes with the according errors. The log likelihood ratio of these two fluxes will then lead to an to be expected significance of the prompt flux.

For the significance analyses the log likelihood ratio method introduced by Li and Ma [LM83] will be used. How this method can be extended to histograms is explained in [Chi13]. The formula for the likelihood ratio per bin i, rewritten for our purpose, is

$$\mathcal{L}_i = \left(\frac{t_{\text{total}} + t_{\text{conv}}}{t_{\text{total}}} \frac{N_{\text{total}}}{N_{\text{total}} + N_{\text{conv}}} \right)^{N_{\text{total}}} \cdot \left(\frac{t_{\text{total}} + t_{\text{conv}}}{t_{\text{conv}}} \frac{N_{\text{conv}}}{N_{\text{total}} + N_{\text{conv}}} \right)^{N_{\text{conv}}} \tag{5.1}$$

where t_{total} is the time over which the total flux is measured and N_{total} the respective count whereas t_{conv} is the time for which the conventional flux is calculated and N_{conv} the predicted flux. The formula for the whole histogram it is simply

$$\mathcal{L} = \prod_i \mathcal{L}_i. \tag{5.2}$$

The significance S can easily be calculated from that expression and is

$$S = \sqrt{-2 \ln \mathcal{L}}. \tag{5.3}$$

To account for the errors on both the total and conventional flux a method that was

originally invented to deal with Monte Carlo weight errors was adopted from [BZ12]. The concept introduced there is called *equivalent number of unweighted events* and we adopt it as *equivalent number of events with Poisson error only*. What this means is that for each count N with an error ΔN we will calculate a count $\tilde{N}$ with the same statistical significance and a Poisson error only. This concept reduces to the simple formula

$$\tilde{N} = \frac{N^2}{\Delta N^2}. \tag{5.4}$$

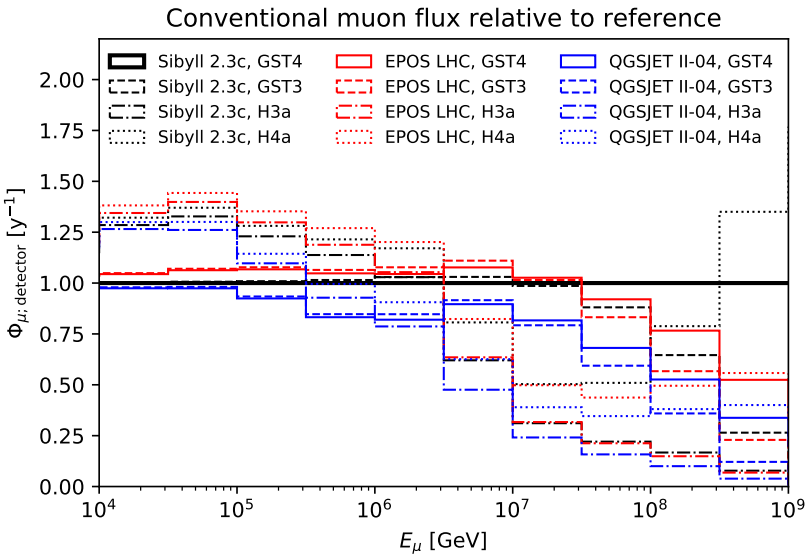

Figure 5.12: Comparison of the energy distributions above 10 TeV of the conventional muon flux at the KM3NeT/ARCA detector for all the different combinations of primary flux and interaction models discussed before. Shown is the flux calculated with different models compared the the flux calculation when using the reference models GST 4-gen and Sibyll 2.3c. The KM3NeT-Std atmosphere was used.

For the significance analysis we assume the following errors for the fluxes: For the conventional flux a general error of at least 20% is assumed but as we have seen in previous sections this sometimes is not enough. Thus we will deduce an error estimate from the different energy and interaction models discussed before. Figure 5.12 shows a comparison of all the different combinations for which the deviation from reference models Sibyll 2.3c and GST 4-gen was calculated. If the thus obtained error is larger than 20% it will be used in the analysis.

For the total flux which is assumed to be measured the errors on the KM3NeT/ARCA energy resolution discussed at the end of chapter 3 were used. Since it does not make much sense to have a binning finer than the detector's energy resolution, four bins were

combined to one. The thus obtained energy histogram is shown in Figure 5.13.

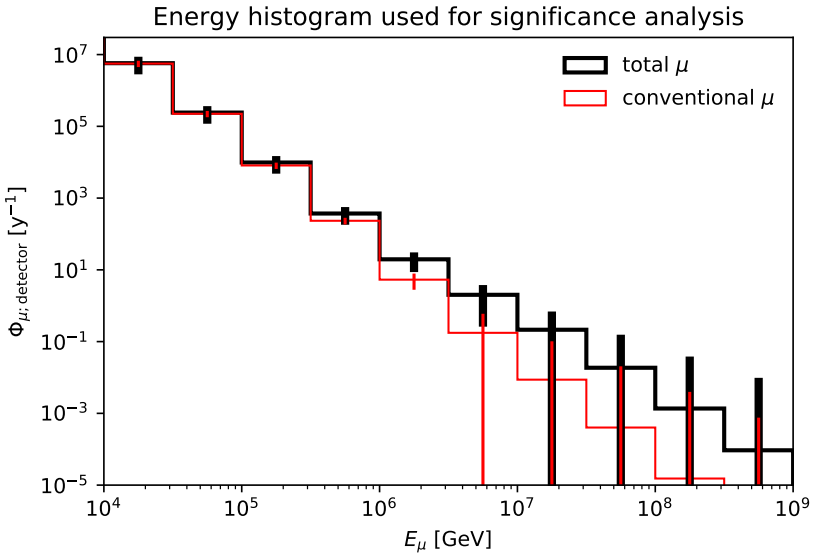

Figure 5.13: The muon energy distribution at the KM3NeT/ARCA detector above 10 TeV with a by four reduced bin number. The models used here are GST 4-gen, NRLMSISE-00, and Sibyll 2.3c. Errors are assigned as describe in the text.

The errors on the five right bins are quite large and they might not all be taken into account in the analysis. Bins are only taken into account if at least one muon is expected in the chosen time interval such that the Poisson error is not larger than the bin itself. Different bin sizes were tested but combining four of the by MCEq predefined bins together leads to the best result.

The final result of the significance analysis is shown in Figure 5.14. The calculated significance has two jumps, at less than one and at around five years. The reason for this is that at these points an additional bin whose expected count reached one was taken into account. A function was fit through the data to get to a smooth result. A significance of 3σ might already be in reach after two years of running the detector. But in all this one should of course not forget that all this is under the strong assumption that all the muons arriving together in a bundle can be resolved. This is certainly one point where this analysis needs improvement.

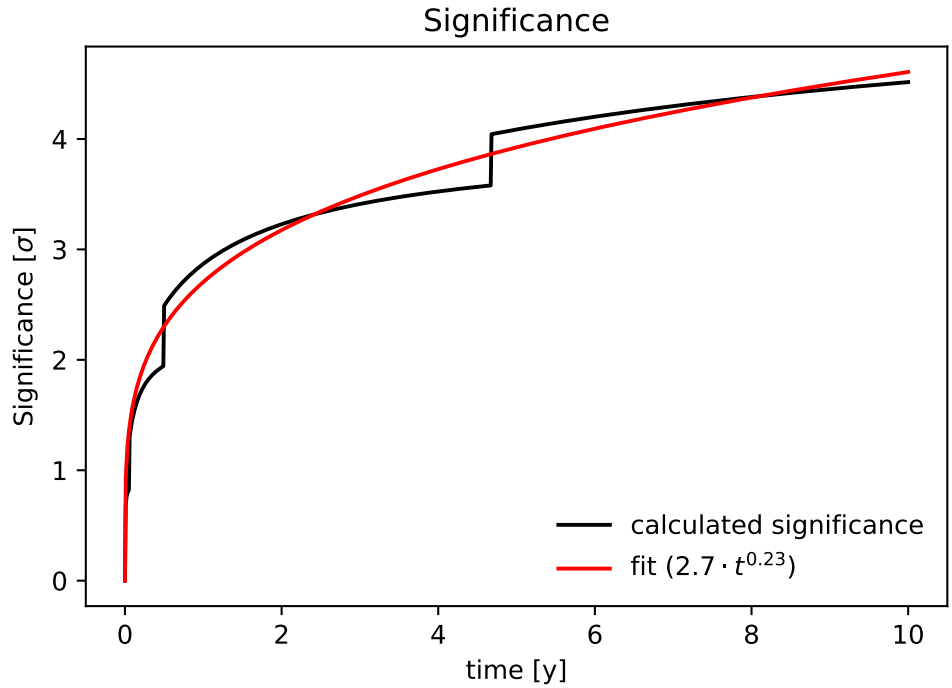

Figure 5.14: Estimate of the significance with which KM3NeT might be able to measure the prompt muon flux after certain times.

Chapter 6

Conclusion

Several calculations of the atmospheric muon flux were presented and discussed in this thesis and some interesting things were found. The first thing to mention, which is not a physical result but important nonetheless, was already found in subsection 4.5.2: The calculations of the extended MCEq agree well with the by far more complex Corsika production and its additional further processing.

The first actual result was that the prompt component plays an important role at the upper end of the muon energy distribution at the detector level and that this should be measurable for KM3NeT/ARCA. In this and all that follows it is, certainly overly optimistic, assumed that all muons in a bundle can be resolved.

The zenith angle distribution was the next thing that was studied. Here the utterly unsurprising result hat the flux gets lower with growing zenith angle was found. Different from the energy in the case of the angular distribution no region where the prompt flux becomes important could be identified.

Also investigated were the fluctuations in muon flux depending on the season. What was found is that the variations can be expected to be small, around 1.67%, much smaller than the 10% that were measured for the atmospheric neutrino flux by IceCube.

In the last section the main question of this work was addressed, namely whether KM3NeT/ARCA will be able to measure the prompt muon flux. In ordner to find an answer to this question a significance analysis was performed where detector and simulation errors were taken into account. From this it was found that a measurement of the prompt muon flux with a significance of 3σ seems possible for KM3NeT – under the assumption that muons in bundles can be resolved.

Having said all that, it should be clear that a lot can still be improved in the analyses. First and foremost, this cannot be mentioned often enough, it needs to be taken into account that muons arrive in bundles of up to a few hundreds which can not all be separated. Secondly, it was found that the prompt flux plays a role for high energies or also large zenith angles where the fluxes are relatively low. Sometimes even that low that the muon flux produced by atmospheric neutrinos cannot be neglected any longer. Thus

a future analysis should include this contribution.

Even though it is impressive what good results can be reached with such a simple energy loss function, there is room for improvement because critical energy losses are not accounted for as it is at the moment. The primary flux models are already some years old and new, data-driven, approaches were developed to describe the flux. A similar work is under way for interaction cross sections and particle yields. One would be well advised to use these models as soon as they are available since besides more recent data they also provide the analyser with an error. Speaking of which: More sophisticated methods for error estimates then the one used here were developed [Bar+06]. Future analyses should probably use these method to get an improved estimate of the errors involved.

References

[Aar+15] M. G. Aartsen et al. "A combined maximum-likelihood analysis of the high-energy astrophysical neutrino flux measured with IceCube". In: *The Astrophysical Journal* 809.1 (2015), p. 98.

[Adr+11] O. Adriani et al. "PAMELA measurements of cosmic-ray proton and helium spectra". In: *arXiv preprint arXiv:1103.4055* (2011).

[Age+11] M. Ageron et al. "ANTARES: the first undersea neutrino telescope". In: *Nuclear Instruments and Methods in Physics Research Section A: Accelerators, Spectrometers, Detectors and Associated Equipment* 656.1 (2011), pp. 11–38.

[Ahn+09] E.-J. Ahn et al. "Cosmic ray interaction event generator SIBYLL 2.1". In: *Physical Review D* 80.9 (2009), p. 094003.

[Ahn+10] H. S. Ahn et al. "Discrepant hardening observed in cosmic-ray elemental spectra". In: *The Astrophysical Journal Letters* 714.1 (2010), p. L89.

[AM+16] S. Adrián-Martínez et al. "Letter of intent for KM3NeT 2.0". In: *Journal of Physics G: Nuclear and Particle Physics* 43.8 (2016), p. 084001.

[An+18] F. P. An et al. "Seasonal variation of the underground cosmic muon flux observed at Daya Bay". In: *Journal of Cosmology and Astroparticle Physics* 2018.01 (2018), p. 001.

[Ane+08] G. Anelli et al. "The totem experiment at the cern large hadron collider". In: *Journal of Instrumentation* 3.08 (2008), S08007.

[Ant+97] P. Antonioli et al. "A three-dimensional code for muon propagation through the rock: MUSIC". In: *Astroparticle Physics* 7.4 (1997), pp. 357–368.

[Ape+11] W. D. Apel et al. "Kneelike structure in the spectrum of the heavy component of cosmic rays observed with KASCADE-Grande". In: *Physical Review Letters* 107.17 (2011), p. 171104.

[Bar+06] G. D. Barr et al. "Uncertainties in atmospheric neutrino fluxes". In: *Physical Review D* 74.9 (2006), p. 094009.

[Bar+52] P. H. Barrett et al. "Interpretation of cosmic-ray measurements far underground". In: *Reviews of Modern Physics* 24.3 (1952), p. 133.

[BZ12] G. Bohm and G. Zech. "Comparison of experimental data to Monte Carlo simulation—Parameter estimation and goodness-of-fit testing with weighted events". In: *Nuclear Instruments and Methods in Physics Research Section A: Accelerators, Spectrometers, Detectors and Associated Equipment* 691 (2012), pp. 171–177.

[Cap+94] A. Capella et al. "Dual parton model". In: *Physics Reports* 236.4-5 (1994), pp. 225–329.

[Chi13] D. Chirkin. "Likelihood description for comparing data with simulation of limited statistics". In: *arXiv preprint arXiv:1304.0735* (2013).

[Dem+17] R. Dembinski H.and Engel et al. "Data-driven model of the cosmic-ray flux and mass composition from 10 GeV to 10 11 GeV". In: *arXiv preprint arXiv:1711.11432* (2017).

[Des11] P. Desiati. "Seasonal Variations of High Energy Cosmic Ray Muons Observed by the IceCube Observatory as a Probe of Kaon/Pion Ratio". In: *International Cosmic Ray Conference*. Vol. 1. 2011, p. 78.

[DG10] P. Desiati and T. K. Gaisser. "Seasonal variation of atmospheric leptons as a probe of charm". In: *Physical review letters* 105.12 (2010), p. 121102.

[Eng+17] R. Engel et al. "The hadronic interaction model Sibyll–past, present and future". In: *EPJ Web of Conferences*. Vol. 145. EDP Sciences. 2017, p. 08001.

[ERS08] R. Enberg, M. H. Reno, and I. Sarcevic. "Prompt neutrino fluxes from atmospheric charm". In: *Physical Review D* 78.4 (2008), p. 043005.

[FE15] A. Fedynitch and R. Engel. "Revision of the high energy hadronic interaction models PHOJET/DPMJET-III". In: (2015).

[Fed+15] A. Fedynitch et al. "Calculation of conventional and prompt lepton fluxes at very high energy". In: *EPJ Web of Conferences*. Vol. 99. EDP Sciences. 2015, p. 08001.

[For47] M. Forro. "Temperature Effect of Cosmic Radiation at 1000-M Water Equivalent Depth". In: *Physical Review* 72.9 (1947), p. 868.

[FTD12] A. Fedynitch, J. B. Tjus, and P. Desiati. "Influence of hadronic interaction models and the cosmic ray spectrum on the high energy atmospheric muon and neutrino flux". In: *Physical Review D* 86.11 (2012), p. 114024.

[Gai] T. Gaisser. "Seasonal variation of atmospheric neutrinos in IceCube". In: *Proceedings, 33rd International Cosmic Ray Conference (ICRC2013): Rio de Janeiro, Brazil, July 2-9, 2013*, p. 0492.

[Gai12] T. K. Gaisser. "Spectrum of cosmic-ray nucleons, kaon production, and the atmospheric muon charge ratio". In: *Astroparticle Physics* 35.12 (2012), pp. 801–806.

[Gai13] T. K. Gaisser. "Atmospheric leptons-the search for a prompt component". In: *EPJ Web of Conferences*. Vol. 52. EDP Sciences. 2013, p. 09004.

[Gar16] Fedynitch A. Garcia R. A. *Muon energy loss in dense media*. `https://www-zeuthen.desy.de/students/2016/Summerstudents2016/reports/RafaelAlvarez.pdf`. [Online; accessed 2018/03/16]. 2016.

[GER16] T. K. Gaisser, R. Engel, and E. Resconi. *Cosmic rays and particle physics*. Cambridge University Press, 2016.

[GMS01] D. E. Groom, N. V. Mokhov, and S. I. Striganov. "Muon stopping power and range tables 10 MeV–100 TeV". In: *Atomic Data and Nuclear Data Tables* 78.2 (2001), pp. 183–356.

[Gri68] V. N. Gribov. "A reggeon diagram technique". In: *Sov. Phys. JETP* 26.414-422 (1968), p. 27.

[Gru05] C. Grupen. *Astroparticle physics*. Springer Science & Business Media, 2005.

[GS13] T. K. Gaisser and S. Stanev T.and Tilav. "Cosmic ray energy spectrum from measurements of air showers". In: *Frontiers of Physics* 8.6 (2013), pp. 748–758.

[Hec+98] D. Heck et al. *CORSIKA: A Monte Carlo code to simulate extensive air showers*. Tech. rep. 1998.

[Hec01] D. Heck. "Extensive air shower simulations with CORSIKA and the influence of high-energy hadronic interaction models". In: *arXiv preprint astro-ph/0103073* (2001).

[Hei17] T. G. G. Heid. "Characterizing the diffuse neutrino flux with the future KM3NeT/ARCA detector". PhD thesis. FAU Erlangen-Nuremberg, 2017.

[Hes12] V. F Hess. "Über Beobachtungen der durchdringenden Strahlung bei sieben Freiballonfahrten". In: *Phys. Z.* 13 (1912), pp. 1084–1091.

[Hil06] A. M. Hillas. "Cosmic rays: Recent progress and some current questions". In: *arXiv preprint astro-ph/0607109* (2006).

[Hon+15a] M. Honda et al. "Atmospheric neutrino flux calculation using the NRLMSISE-00 atmospheric model". In: *Physical Review D* 92.2 (2015), p. 023004.

[Hon+15b] M. Honda et al. "Atmospheric neutrino flux calculation using the NRLMSISE-00 atmospheric model". In: *Physical Review D* 92.2 (2015), p. 023004.

[Hon+17] M. Honda et al. "Calculation Of Atmospheric Neutrino Flux Based On AMS02 Observations". In: *PoS* ICRC2017 (2017), p. 1022.

[Hon+95] M. Honda et al. "Calculation of the flux of atmospheric neutrinos". In: *Physical Review D* 52.9 (1995), p. 4985.

[Ill+11] J.I Illana et al. "Atmospheric lepton fluxes at very high energy". In: *Astroparticle Physics* 34.9 (2011), pp. 663–673.

[IMM09] J. I. Illana, M. Masip, and D. Meloni. "Atmospheric lepton fluxes at ultra-high energies". In: *Journal of Cosmology and Astroparticle Physics* 2009.09 (2009), p. 008.

[Kei+04] B. Keilhauer et al. “Impact of varying atmospheric profiles on extensive air shower observation: atmospheric density and primary mass reconstruction”. In: *Astroparticle Physics* 22.3-4 (2004), pp. 249–261.

[Klo16] B. Klose. *Meteorologie: eine interdisziplinäre Einführung in die Physik der Atmosphäre*. Springer-Verlag, 2016.

[KOP97] N. N. Kalmykov, S. S. Ostapchenko, and A. I. Pavlov. “Quark-gluon-string model and EAS simulation problems at ultra-high energies”. In: *Nuclear Physics B-Proceedings Supplements* 52.3 (1997), pp. 17–28.

[KP71] R. P. Kokoulin and A. A. Petrukhin. “Influence of the Nuclear Form Factor on the Cross Section of Electron Pair Production by High Energy Muons”. In: *pp 2436-45 of 12th International Conference on Cosmic Rays. Vol. 6. Hobart, Australia International Union of Pure and Applied Physics (1971).* Inst. of Engineering-Physics, Moscow. 1971.

[KS12] U. F. Katz and Ch. Spiering. “High-energy neutrino astrophysics: Status and perspectives”. In: *Progress in Particle and Nuclear Physics* 67.3 (2012), pp. 651–704.

[LM83] T.-.P Li and Y.-Q. Ma. “Analysis methods for results in gamma-ray astronomy”. In: *The Astrophysical Journal* 272 (1983), pp. 317–324.

[Msia] *NRLMSISE-00.* `https://en.wikipedia.org/wiki/NRLMSISE-00`. Accessed: 2018/04/09.

[Msib] *NRLMSISE-00 Model 2001.* `https://ccmc.gsfc.nasa.gov/modelweb/atmos/nrlmsise00.html`. Accessed: 2018/04/09.

[oa76] National oceanic and atmospheric administration. “Atmosphere, US Standard”. In: *National Aeronautics and Space Administration, United States Air Force, Washington, DC* (1976).

[Ost11] S. Ostapchenko. “Monte Carlo treatment of hadronic interactions in enhanced Pomeron scheme: QGSJET-II model”. In: *Physical Review D* 83.1 (2011), p. 014018.

[PDG+14] Olive K. A. PDG et al. “Particle Physics Booklet Chin”. In: *Phys. C* 38 (2014), p. 090001.

[PDG16] C. Patrignani *et al.* (Particle Data Group). “Review of particle physics”. In: *Chinese physics C* 40.10 (2016). 2017 update, p. 100001.

[Pet61] B. Peters. “Primary cosmic radiation and extensive air showers”. In: *Il Nuovo Cimento (1955-1965)* 22.4 (1961), pp. 800–819.

[Pic+02] J. M. Picone et al. “NRLMSISE-00 empirical model of the atmosphere: Statistical comparisons and scientific issues”. In: *Journal of Geophysical Research: Space Physics* 107.A12 (2002).

[Pie+15] T. Pierog et al. “EPOS LHC: Test of collective hadronization with data measured at the CERN Large Hadron Collider”. In: *Physical Review C* 92.3 (2015), p. 034906.

[RER01] S. Roesler, R. Engel, and J. Ranft. "The monte carlo event generator dpmjet-iii". In: *Advanced Monte Carlo for Radiation Physics, Particle Transport Simulation and Applications*. Springer, 2001, pp. 1033–1038.

[Rie+15a] F. Riehn et al. "A new version of the event generator Sibyll". In: *arXiv preprint arXiv:1510.00568* (2015).

[Rie+15b] F. Riehn et al. "Charm production in SIBYLL". In: *EPJ Web of Conferences*. Vol. 99. EDP Sciences. 2015, p. 12001.

[Rie+17] F. Riehn et al. "The hadronic interaction model SIBYLL 2.3 c and Feynman scaling". In: *arXiv preprint arXiv:1709.07227* (2017).

[Roc09] D. Rocco. *Seasonal Variations in Muon Rate with Ice-Cube*. 2009.

[Sch17] F. G. Schröder. "Radio detection of cosmic-ray air showers and high-energy neutrinos". In: *Progress in Particle and Nuclear Physics* 93 (2017), pp. 1–68.

[TIG96] M. Thunman, G. Ingelman, and P. Gondolo. "Charm production and high energy atmospheric muon and neutrino fluxes". In: *Astroparticle Physics* 5.3-4 (1996), pp. 309–332.

[Til+10] S. Tilav et al. *Atmospheric Variations as observed by IceCube*. 2010.

Hiermit versichere ich, dass ich die vorliegende Masterarbeit erstmalig einreiche, selbständig verfasst und keine anderen als die angegebenen Quellen und Hilfsmittel verwendet habe.